Precise Modeling and Design of Self-Resonant for High-Efficiency Mid-Range Wireless Power Transfer System

Lei Zhu, *Student Member, IEEE*, Laili Wang, *Senior Member, IEEE*, Min Wu, *Student Member, IEEE*, Chenxu Zhao, *Student Member, IEEE*, and Longyang Yu, *Student Member, IEEE*

***Abstract*—Transfer power and efficiency of wireless power transfer (WPT) systems are limited by the quality factor and coupling coefficient of the transmitting (Tx) coil and receiving (Rx) coil. Getting rid of compensation circuits, self-resonant coils have simple structure, high system reliability, high quality factor and high power level, making it a promising candidate for WPT applications. In modeling and computation of self-resonant coils, the results derived from the transmission line theory have obvious errors, and the finite element simulation takes a long computing time. For obtaining accurate results and achieving fast computation, a partial-element equivalent circuit (PEEC) method is applied to calculate the self-resonant frequency (SRF) and the current distribution of helical coils. To validate the accuracy of the proposed model, some prototypes were simulated and measured. The theoretical calculation predications are in great agreements with the simulation and measurement results. The magnetic coupling model between Tx and Rx is also established using PEEC method and a novel design guideline of self-resonant helical coils is proposed. Furthermore, a WPT system with 6.78 MHz self-resonant helical coils was designed, fabricated and tested for a high-efficiency mid-range energy transfer. It was used to drive a 5W load wirelessly as a demonstration to validate the feasibility of the proposed system in practical applications.**

***Index Terms*—Coils, energy efficiency, magnetic resonance, wireless power transmission.**

I. Introduction

WIRELESS power transfer (WPT) technology has been studied and applicated extensively in many applications including biomedical implants, consumer electronics, household applications and electric vehicles [1], [2], [3], [4] in recent years for its convenience, reliability and safety. WPT can be realized through mechanic [5] or electromagnetic methods. Compared with mechanic methods, electromagnetic methods have advantages in simpler system structure, longer transfer distance and higher energy efficiency, which receive more attention from researchers. There are two major categories of electromagnetic WPT: radiative WPT and nonradiative WPT [6]. The radiative WPT consisting of microwave power transfer and optical power transfer [7], [8], [9], can transmit energy over a long distance that at the level of meters to kilometers, but is low efficient, costly, surrounding sensitive and environmentally unfriendly. Contrary to radiative WPT, the nonradiative WPT utilizing electronic field or magnetic field has simple structure, high efficiency and is insensitive to surrounding changes. The electric field can only be used in specific situations because it's harmful to human body, while the WPT employing magnetic field is safe to use in daily life and widely known as inductive power transfer (IPT) [10], [11].

However, the transfer distance of IPT is still limited to short-range, because the efficiency decreases sharply as the transfer distance increases. In 2007, a research team from Massachusetts Institute of Technology (MIT) demonstrated an efficient nonradiative WPT system that lighted a 60W lightbulb over a distance of 2m using self-resonant coils in a strongly coupled regime [12]. Since the great achievement of MIT, researches on mid-range (the transfer distance is larger than the coil diameter) WPT [13], [14], [15] based on self-resonant coils have been on rise. To distinguish from traditional IPT, this kind of IPT is called as magnetic resonant power transfer (MRPT), which utilizes self-resonant coils instead of traditional coils accompanying with lumped compensation networks. Similar to traditional IPT, the MRPT system is composed of a power source, a DC/AC converter, a transmitting (Tx) coil, a receiving (Rx) coil, an AC/DC converter and a load. The transfer power and efficiency of IPT system is determined by the quality factor and coupling coefficient of coils [16], [17]. As the frequency increases, the quality factor of coil is improved. With the development of wide-bandgap semiconductors [18], [19], power electronic converters can operate efficiently at MHz [20]. Getting rid of lumped resonant capacitors, the quality factor Q of self-resonant coils are improved remarkably at high frequency and the traditional lumped inductance model of coil is no longer applicable. In this sense, self-resonant coils are critical components of MRPT system, and the modeling and design of self-resonant coils is essential.

At low frequency, the parasitic capacitances between turns can be ignored, so the coil can be equivalent to a lumped inductance. However, as the frequency increases, the influence of parasitic

Manuscript received 24 March 2022; revised 17 July 2022, 26 September 2022, and 25 December 2022; accepted 26 January 2023. Date of publication 13 February 2023; date of current version 20 April 2023. This work was supported by HPC Platform, Xi'an Jiaotong University. Recommended for publication by Associate Editor O. C. Onar. *(Corresponding author: Laili Wang.)*

The authors are with the State Key Laboratory of Electrical Insulation and Power Equipment, Xi'an Jiaotong University, Xi'an 710049, China (e-mail: jasmine@stu.xjtu.edu.cn; llwang@mail.xjtu.edu.cn; wm3117079009@stu.xjtu.edu.cn; zhaochenxu@stu.xjtu.edu.cn; yulongyang@xidian.edu.cn).

Color versions of one or more figures in this article are available at https://doi.org/10.1109/TPEL.2023.3243379.

Digital Object Identifier 10.1109/TPEL.2023.3243379

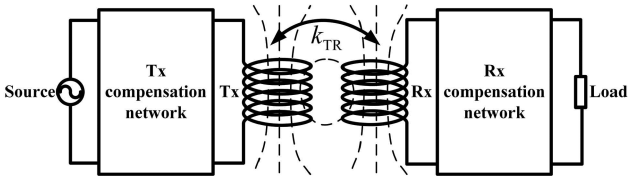

Fig. 1. Model of typical IPT system.

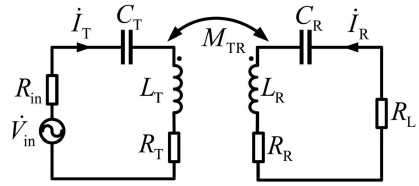

Fig. 2. Equivalent circuit of IPT system with series-series compensation network.

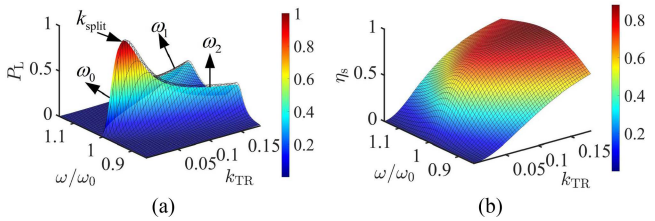

Fig. 3. (a) Normalized output power P_L and (b) energy efficiency η_s versus coupling coefficient k_{TR} and normalized angular frequency ω/ω_0.

capacitances becomes non-negligible and the current distribution along the coil is no longer identical when the wavelength of the electromagnetic wave is comparable with the line length. In this case, the traditional lumped element theory is no longer applicable. Paper [21] presented empirical formulas to estimate the self-resonant frequency (SRF) of Archimedean spiral coils and helical coils, and paper [22], [23], [24] developed an analytical model based on results from literatures of inductance and stray capacitance. However, these models can only give the first SRF and cannot get the current distribution along the coil. The transmission line theory was widely applied to self-resonant coils to get the SRF and current distribution [25], [26], [27], [28], which ignored the influence of the coil structure and resulted in great errors. In this paper, we model the helical coil using partial-element equivalent circuit (PEEC) method [29], [30] to deduce SRFs and current distribution for accurate results and fast computation.

The rest of this article is organized as follows. Section II introduces the typical structure of IPT system and its equivalent circuit, describing transfer characteristics of IPT system. In Section III, high frequency characteristics of self-resonant coil are discussed using lossless uniform two-conductor transmission line model. Afterwards, a precise model of PEEC is built to calculated the SRFs and current distributions. The magnetic coupling mechanism between Tx and Rx is modeled in Section IV. A demonstration of high-efficient mid-range WPT system is illustrated with self-resonant helical coils working at 6.78 MHz in section V. Finally, Section VI concludes this article.

II. Typical IPT System and Transfer Characteristics

The structure and characteristic of MRPT system are similar to traditional IPT system, replacing the traditional coil and its compensation network by a self-resonant coil. Recent researches show that the operation principle of MPRT has no difference from that of IPT and can be analyzed using the standard electric circuit theory [31], [32]. Usually, the self-resonant coil is equivalent to a lumped LC series or parallel resonant network, because the terminal reactance of self-resonant coil is zero or infinite at SRFs. And series resonance is more commonly used in practical applications.

IPT system is composed of a source, a Tx coil with a Tx compensation network, a Rx coil with a Rx compensation network and a load, as shown in Fig. 1. The equivalent circuit of a typical IPT system with series-series compensation networks is shown in Fig. 2. The voltage source $\dot{V}_S$ is used as a power supply. L_T and L_R are the self-inductance of Tx and Rx, respectively, and M_{TR} is the mutual inductance between Tx and Rx. R_T and R_R are the parasitic resistance of Tx and Rx, respectively. C_T and C_R are the resonant capacitance connected to Tx and Rx. R_L is the equivalent load resistance connected to Rx.

Applying Kirchhoff's Voltage Law to Tx and Rx circuit, the standard coupled circuit (1) is obtained.

$$\begin{bmatrix} \dot{V}_S \\ 0 \end{bmatrix} = \begin{bmatrix} R_S + Z_T & j\omega M_{TR} \\ j\omega M_{TR} & Z_R + R_L \end{bmatrix} \begin{bmatrix} \dot{I}_T \\ \dot{I}_R \end{bmatrix} \tag{1}$$

with

$$\begin{cases} Z_T = R_T + j\omega L_T + 1/j\omega C_T \\ Z_R = R_R + j\omega L_R + 1/j\omega C_R \end{cases} \tag{2}$$

where ω is the operating frequency. The current $\dot{I}_T$ and $\dot{I}_R$ flowing through Tx and Rx are solved from (1) and can be written as

$$\begin{cases} \dot{I}_T = \dfrac{\dot{V}_S}{R_S + Z_T + \omega^2 M_{TR}^2/(Z_R + R_L)} \\ \dot{I}_R = -\dfrac{j\omega M_{TR}\dot{V}_S}{(R_S + Z_T)(Z_R + R_L) + \omega^2 M_{TR}^2} \end{cases} \tag{3}$$

The output power P_L can be calculated by $P_L = I_R^2 R_L$. The relationship of the normalized output power P_L with the coupling coefficient k_{TR} and the normalized angular frequency ω/ω_0 is shown in Fig. 3(a). $k_{TR} = M_{TR}/\sqrt{L_T L_R}$ is the coupling coefficient between Tx and Rx and $\omega_0 = 1/\sqrt{L_T C_T} = 1/\sqrt{L_R C_R}$ is the resonant frequency decided by the inductance and resonant capacitance. When the coupling coefficient k_{TR} is less than the critical coupling coefficient k_{split}, the output power P_L reaches its maximum value at the resonant frequency ω_0. When k_{TR} is large than k_{split}, the frequency splitting phenomenon occurs and the output power P_L reaches its maximum value at two splitting frequencies ω_{12}. The energy efficiency can be calculated by $\eta_s = P_L / \mathrm{Re}[\dot{V}_S \dot{I}_T^*]$. Fig. 3(b) shows the relationship of the energy efficiency η_s with the coupling coefficient k_{TR} and the normalized angular frequency ω/ω_0.

In mid-range WPT, the coupling coefficient is very low and the operating frequency ω is set at resonant frequency ω_0 to maximize the output power and efficiency. Working at resonant

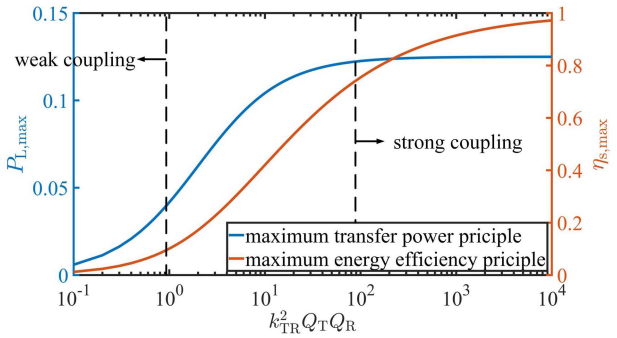

Fig. 4. Maximum transfer power $P_{\mathrm{L,max}}$ and maximum energy efficiency $\eta_{\mathrm{s,max}}$ of series-series IPT system versus $k_{\mathrm{TR}}^2 Q_{\mathrm{T}} Q_{\mathrm{R}}$.

frequency, the current $\dot{I}_{\mathrm{T}}$ and $\dot{I}_{\mathrm{R}}$ in (1) and can be written as

$$\begin{cases} \dot{I}_{\mathrm{T}} = \dfrac{\dot{V}_{\mathrm{S}}}{R_{\mathrm{S}} + R_{\mathrm{T}} + \omega_0^2 M_{\mathrm{TR}}^2 / (R_{\mathrm{R}} + R_{\mathrm{L}})} \\ \dot{I}_{\mathrm{R}} = -\dfrac{j\omega_0 M_{\mathrm{TR}} \dot{V}_{\mathrm{S}}}{(R_{\mathrm{S}} + R_{\mathrm{T}})(R_{\mathrm{R}} + R_{\mathrm{L}}) + \omega_0^2 M_{\mathrm{TR}}^2} \end{cases} \tag{4}$$

In different application scenarios, the IPT system can operate with maximum power transfer principle or maximum energy efficiency principle to meet different requirements. The maximum power transfer principle is designed to maximize the power P_{L} delivered to the load. The maximum transfer power $P_{\mathrm{L,max}}$ can be calculated by (5). The maximum energy efficiency principle is aiming to maximize the system energy efficiency η_{s}. The maximum energy efficiency $\eta_{\mathrm{s,max}}$ can be calculated by (6).

$$P_{\mathrm{L,max}} = \frac{V_{\mathrm{S}}^2}{R_{\mathrm{in}} + R_{\mathrm{T}}} \frac{k_{\mathrm{TR}}^2 Q_{\mathrm{T}} Q_{\mathrm{R}}}{4\left[(R_{\mathrm{S}}/R_{\mathrm{T}} + 1) + k_{\mathrm{TR}}^2 Q_{\mathrm{T}} Q_{\mathrm{R}}\right]} \tag{5}$$

$$\eta_{\mathrm{s,max}} = \frac{k_{\mathrm{TR}}^2 Q_{\mathrm{T}} Q_{\mathrm{R}} / (R_{\mathrm{S}}/R_{\mathrm{T}} + 1)}{\left[1 + \sqrt{1 + k_{\mathrm{TR}}^2 Q_{\mathrm{T}} Q_{\mathrm{R}} / (R_{\mathrm{S}}/R_{\mathrm{T}} + 1)}\right]^2} \tag{6}$$

where $Q_{\mathrm{T}} = \omega_0 L_{\mathrm{T}}/R_{\mathrm{T}}$ and $Q_{\mathrm{R}} = \omega_0 L_{\mathrm{R}}/R_{\mathrm{R}}$ are the unload quality factor of Tx and Rx, respectively. It can be concluded from (5) and (6) that the maximum transfer power $P_{\mathrm{L,max}}$ and maximum energy efficiency $\eta_{\mathrm{s,max}}$ increase with $k_{\mathrm{TR}}^2 Q_{\mathrm{T}} Q_{\mathrm{R}}$. And Fig. 4 shows the variation trend of $P_{\mathrm{L,max}}$ and $\eta_{\mathrm{s,max}}$ with $k_{\mathrm{TR}}^2 Q_{\mathrm{T}} Q_{\mathrm{R}}$. The coupling coefficient k_{TR} mainly depends on the distance between Tx and Rx which decided by application requirements. In order to maintain greater transfer power and efficiency in mid-range, it is very necessary to improve the unload quality factor Q_0 of the coil.

Compared with traditional resonant network composed of a coil compensated with lumped resonant capacitor, the self-resonant coil has following advantages: simple structure, light weight and high reliability. Additionally, getting rid of compensation capacitor, the unload quality factor Q_0 of self-resonant coil is significantly increased because power losses of capacitor and solder joints are avoided. And the transfer power capability is enhanced because there is no limit by the rated voltage of compensation capacitor. Therefore, the self-resonant coil has great advantages in high-power level and high-efficiency for mid-range WPT applications.

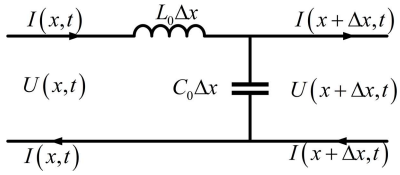

Fig. 5. Model of a lossless uniform two-conductor transmission line of length Δx.

In this section, the self-resonant coil is modeled as a lumped LC resonant network. And the modeling method of traditional IPT system is used to analyze the MRPT system. Through the analysis of transfer power and efficiency, a simple and intuitive understanding of transfer characteristics of MRPT system is obtained. However, it is inaccurate to equate the self-resonant coil to a lumped LC resonant network. Because it only considers the terminal impedance at SRF, but ignores the internal characteristics of the coil. Actually, the current along the coil is not identical at SRF, which has a large impact on transfer power and efficiency. In order to get a more accurate model of MRPT system, the PEEC method is applied in modeling the self-resonant coil and the magnetic coupling mechanism in following sections. The self-resonant coil is modeled as a network of partial elements with distributed parameters. Therefore, the high frequency characteristic of the coil can be described more accurately.

III. Modeling of Self-Resonant Helical Coils

As one of the simplest coils, the helical coil is widely used in MRPT system. When the wire length of the coil is comparable with the wavelength of the electromagnetic wave, the lumped element theory fails. In many papers, the coil is directly equivalent to a straight line and the transmission line theory is used to model the coil. It can help us to have a simple and intuitive understanding of the high-frequency characteristics of the coil, but cannot accurately calculate the SRFs and the current distributions along the coil. In order to accurately describe the coil, a PEEC model is proposed and applied to helical coils in this section.

A. Transmission Line Model

For a lossless uniform two-conductor transmission line as shown in Fig. 5, the variation of voltage and current along the line can be expressed by the telegraph equation as shown in (7).

$$\begin{cases} \partial U/\partial z + L_0 \partial I/\partial t = 0 \\ \partial I/\partial z + C_0 \partial U/\partial t = 0 \end{cases} \tag{7}$$

where L_0 and C_0 is the inductance and capacitance per unit length of the transmission line respectively, which can be solved by static field method. $Z_0 = \sqrt{L_0/C_0}$ is defined as the characteristic impedance of the transmission line.

The general solution of (7) is

$$\begin{cases} U(x,t) = U^+(t - x/v) + U^-(t + x/v) \\ I(x,t) = I^+(t - x/v) - I^-(t + x/v) \end{cases} \tag{8}$$

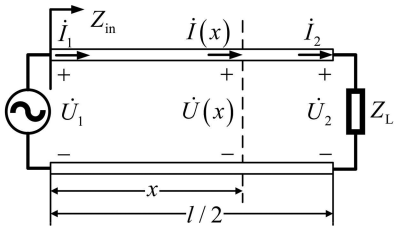

Fig. 6. A two-conductor transmission line connected in the circuit with a terminal impedance Z_L.

where $U^+(t-x/v)$ and $I^+(t-x/v)$ represent the incident voltage wave and the incident current wave propagating in $+x$ direction, respectively. $U^-(t+x/v)$ and $I^-(t+x/v)$ represent the reflected voltage wave and the reflected current wave propagating in -x direction, respectively. $v=1/\sqrt{L_0C_0}$ is the propagation velocity.

Fig. 6 shows a two-conductor transmission line connected in the circuit with a terminal impedance Z_L, where $Z_L=0$ and $Z_L=\infty$ represent a short-end terminal circuit or an open-end terminal circuit, respectively. The input impedance Z_{in} of the transmission line is defined as the ratio of the voltage phasor $\dot{U}_1$ to the current phasor $\dot{I}_1$ at the input terminal.

$$Z_{in}=\frac{\dot{U}_1}{\dot{I}_1}=Z_0\frac{Z_L+jZ_0\tan(\pi fl/c)}{Z_0+jZ_L\tan(\pi fl/c)} \tag{9}$$

where $c=3\times10^8\mathrm{m/s}$ is the velocity of light, f is the frequency of source and $l/2$ is the length of transmission line.

$$\begin{cases} Z_{in}=jZ_0\tan(\pi fl/c)=jX_{in} & \text{short–end} \\ Z_{in}=-jZ_0\cot(\pi fl/c)=jX_{in} & \text{open–end} \end{cases} \tag{10}$$

When the terminal is short-end or open-end, the input impedance is purely reactive as shown in (10). It can be either inductive or capacitive, depending on the value of $\pi fl/c$. The input reactance X_{in} varying with frequency is shown in Fig. 7(a) and Fig. 8(a). When $f=n_i\,c/2l\,(n_i=1,2,3\ldots)$, the input reactance X_{in} is zero or infinite, showing the characteristic of LC series or parallel resonance. Meanwhile, the total reflection phenomenon occurs on the transmission line, where the incident current wave and the reflected current wave are superimposed to form a standing wave. These frequencies are defined as self resonant frequencies. The current distributions along the line at different SRFs are shown in Fig. 7(b)–(e) and Fig. 8(b)–(e).

For a short-end transmission line, the first SRF is a parallel resonant frequency (PF), where the input reactance is infinite, showing the characteristic of LC parallel resonance. And the current distribution along the line at 1st PF is shown in Fig. 7(b), which is a sinusoidal curve. The second SRF is a series resonant frequency (SF), where the input reactance is zero, showing the characteristic of LC series resonance. And the current distribution at 1st SF is shown in Fig. 7(c). When $0<f<$ 1st PF, the input reactance is inductive. When 1st PF $<f<$ 1st SF, the input reactance is capacitive. With the increase of frequency, the input reactance repeats inductive, infinite, capacitive and zero

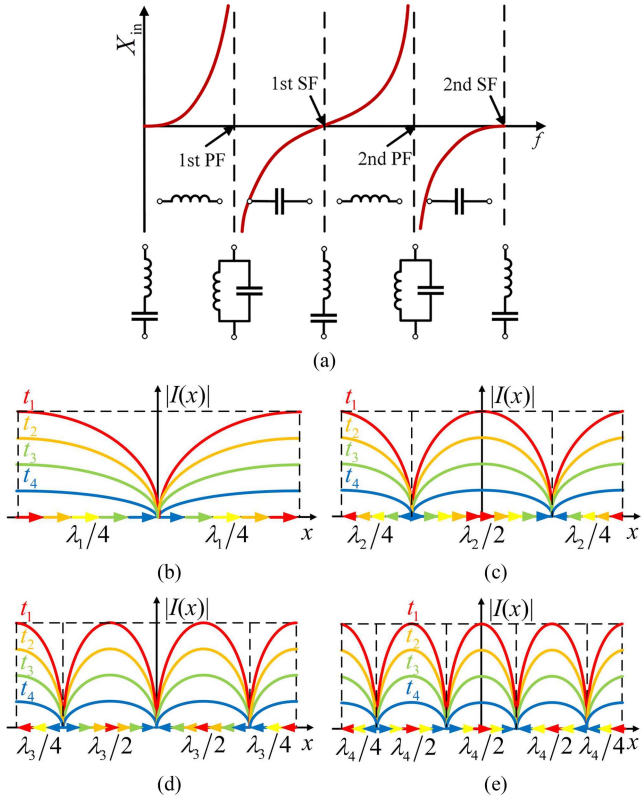

Fig. 7. Characteristics of a short-end transmission line. (a) Input reactance X_{in} versus frequency f. Current distribution waveforms along the line at (b) 1st PF. (c) 1st SF. (d) 2nd PF. (e) 2nd SF.

as shown in Fig. 7(a). In addition, Fig. 7(d) and (e) show the current distribution at 2nd PF and 2nd SF, respectively.

For an open-end transmission line, the frequency range of inductive and capacitive property is just opposite to that of short-end transmission line as shown in Fig. 8(a). The first SRF is a SF and the current distribution at 1st SF is shown in Fig. 8(b). The second SRF is a PF and the current distribution at 1st PF is shown in Fig. 8(c). When $0<f<$ 1st SF, the input reactance is capacitive. When 1st SF $<f<$ 1st PF, the input reactance is inductive. With the increase of frequency, the input reactance repeats capacitive, zero, inductive and infinite as shown in Fig. 8(a). In addition, Fig. 8(d) and (e) show the current distribution at 2nd SF and 2nd PF, respectively.

According to the above analysis, we can get the working mode of a lossless uniform two-conductor transmission line. The working mode of helical coil is similar to that. And some definitions in transmission lines can be applied to self-resonant coils. So, we can have a simple and intuitive understanding of the high frequency characteristics of helical coils. For a short-end helical coil, the first SRF point is a PF point and the second SRF point is a SF point. For an open-end helical coil, the first SRF point is a SF point and the second SRF point is a PF point. The current distribution along the coil is a standing wave. When working at SFs, the input reactance X_{in} is zero and the current at the power source is the maximum. When working at PFs, the input reactance X_{in} is infinite and the current at the power source is zero. However, there are some differences in the values

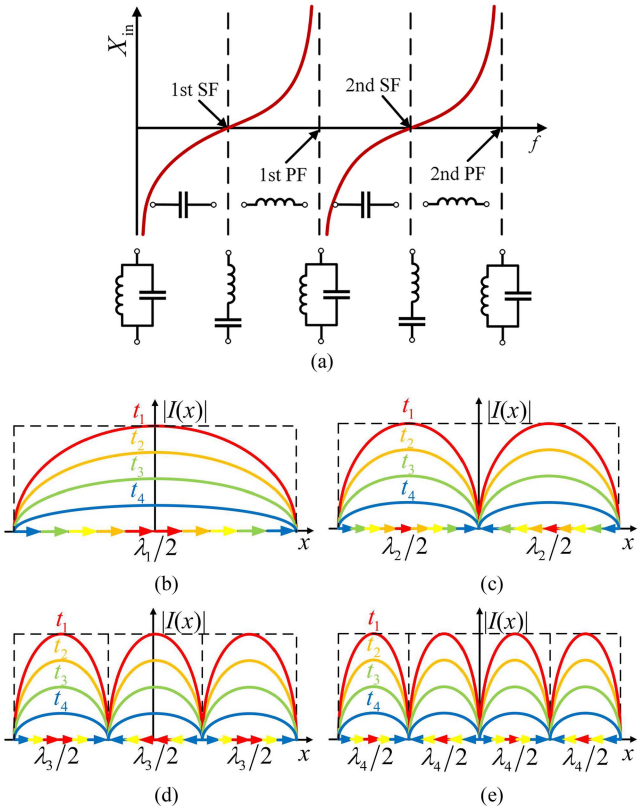

Fig. 8. Characteristics of an open-end transmission line. (a) Input reactance X_{in} versus frequency f. Current distribution waveforms along the line at (b) 1st SF. (c) 1st PF. (d) 2nd SF. (e) 2nd PF.

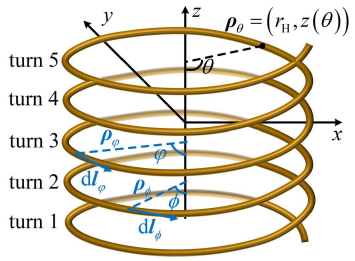

Fig. 9. Simple structure of a helical coil.

of SRFs and the current distribution waveforms caused by the structure of helical coils. In order to solve the SRFs and the current distributions, a PEEC model is established.

B. Distributed Inductance, Capacitance, and Resistance

As shown in Fig. 9, a helical coil can be described by function $\boldsymbol{\rho}_\theta = (r_{\text{H}}, z(\boldsymbol{\theta}))$ in a cylindrical coordinate system, where $\theta \in [0, 2\pi N]$. r_{H} is the radius of the helical coil and $z(\boldsymbol{\theta} + 2\pi) - z(\boldsymbol{\theta})$ is the pitch between two turns at position $\boldsymbol{\theta}$. When $z(\boldsymbol{\theta})$ increases linearly with $\boldsymbol{\theta}$, it becomes the simplest case of Archimedes helical coil whose turn pitch is uniform.

Using Neumann formula, the mutual inductance between segment $[\varphi - \mathrm{d}\varphi, \varphi]$ and segment $[\phi - \mathrm{d}\phi, \phi]$ as shown in Fig. 9

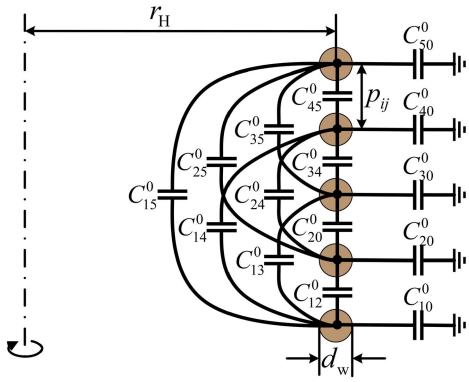

Fig. 10. Vertical section view of a helical coil with distributed capacitance C_{ij}^0.

can be calculated by

$$\begin{aligned} M_{\varphi\phi} &= \frac{\mu_0}{4\pi}\int\int \frac{\mathrm{d}\boldsymbol{l}_\varphi \cdot \mathrm{d}\boldsymbol{l}_\phi}{|\boldsymbol{\rho}_\varphi - \boldsymbol{\rho}_\phi|} \\ &= \frac{\mu_0 r_\varphi r_\phi}{4\pi}\iint \frac{\sin\varphi\sin\phi + \cos\varphi\cos\phi}{\sqrt{{r_\varphi}^2 + {r_\phi}^2 - 2r_\varphi r_\phi\cos(\varphi-\phi) + z_{\varphi\phi}^2}} \\ &\quad \mathrm{d}\phi\mathrm{d}\varphi \\ &= \bar{M}_{\varphi\phi}\mathrm{d}\varphi \end{aligned} \tag{11}$$

where μ_0 is the magnetic permeability of vacuum, r_φ and r_ϕ are equal to r_{H}, and $z_{\varphi\phi} = z(\varphi) - z(\phi)$ is the vertical distance between segment $[\varphi - \mathrm{d}\varphi, \varphi]$ and segment $[\phi - \mathrm{d}\phi, \phi]$. $\bar{M}_{\varphi\phi}$ is defined as the mutual inductance normalized by angle.

The self-inductance of segment $[\varphi - \mathrm{d}\varphi, \varphi]$ is

$$L_\varphi = M_{\varphi\phi}(r_\varphi = r_{\text{H}}, r_\phi = r_\varphi - d_{\text{w}}/2) = \bar{L}_\varphi \mathrm{d}\varphi \tag{12}$$

where $\bar{L}_\varphi$ is defined as the self-inductance normalized by angle.

In order to calculate the capacitance between two turns, the helical coil is considered as a series of coaxial rings. Fig. 10 shows the vertical section view of a series of single-layer air-core coaxial rings with a radius r_{H}, turn number N and turn pitch p_{ij}. The diameter of the wire is d_{w}. Ignoring the insulation thickness, the direct capacitance C_{ij}^0 is generated by the air space between two conductors or between the conductor and the ground can be calculated by the following method.

Assuming that the turn i is uniformly charged with q_i, the linear charge density is τ_i. The potential field $\Phi_{ij}(r_i, r_j, z_{ij})$ on turn j generated by turn i can be calculated by

$$\begin{aligned} \Phi_{ij}(r_i, r_j, z_{ij}) &= \frac{\tau_i}{4\pi\varepsilon_0}\oint \frac{1}{|\boldsymbol{\rho}_i - \boldsymbol{\rho}_j|}\mathrm{d}\boldsymbol{l} \\ &= \frac{q_i}{2\pi^2\varepsilon_0} K(k_{ij}) \Big/ \sqrt{(r_i + r_j)^2 + z_{ij}^2} \\ &= \alpha_{ij} q_i \end{aligned} \tag{13}$$

with

$$k_{ij} = \sqrt{4r_i r_j \Big/ \left[(r_i + r_j)^2 + z_{ij}^2\right]} \tag{14}$$

where ε_0 is the dielectric constant of vacuum. r_i and r_j are equal to r_{H}. In particular, $r_j = r_{\mathrm{H}} - d_{\mathrm{w}}/2$ when $j = i$. α_{ij} is defined as the potential coefficient. $K(k)$ is the complete elliptic integral of the first kind as shown in (15).

$$K(k) = F(k, \pi/2) = \int_0^{\pi/2} 1\Big/\sqrt{1 - k^2 \sin^2 x}\,\mathrm{d}x \tag{15}$$

In matrix notation, (13) can be expressed as

$$\boldsymbol{\Phi} = \boldsymbol{\alpha}\mathbf{q} \tag{16}$$

Rewriting the above equation as the form that charge is a function of potential, (17) is obtained.

$$\mathbf{q} = \boldsymbol{\beta}\boldsymbol{\Phi} = \boldsymbol{\alpha}^{-1}\boldsymbol{\Phi} \tag{17}$$

where β_{ij} is the electrostatic induction coefficient. The direct capacitance C_{ij}^0 can be calculated by

$$C_{ij}^0 = \begin{cases} -\beta_{ij} & i \neq j \\ \sum_{j=1}^{N} \beta_{ij} & i = j \end{cases} \tag{18}$$

The total equivalent capacitance C_{ij} between turn i and j is

$$C_{ij} = C_{ij}^0 + C_{ii}^0 C_{jj}^0 \Big/ \sum_{k=1}^{N} C_{kk}^0 \tag{19}$$

It should be noted that the above equation will produce a large error when the turn spacing is very small, because the other turns will have an effect on the potential field produced by q_i. The normalized distributed capacitance $\bar{C}_{ij}$ is obtained by dividing C_{ij} by 2π.

$$\bar{C}_{ij} = \frac{C_{ij}}{2\pi} = \frac{C_{ij}^0 + C_{ii}^0 C_{jj}^0 \Big/ \sum_{k=1}^{N} C_{kk}^0}{2\pi} \tag{20}$$

The total power loss P_{tot} is consisted of radiation loss P_{rad} and ohmic loss P_{ohm}. For nonradiative WPT, the radiative loss can be ignored, because it's much smaller than ohmic loss. On account of skin effect and proximity effect, the ohmic loss can be given as conduct power loss $P_{\mathrm{cond\ u.l.}}$ and proximity power loss $P_{\mathrm{prox\ u.l.}}$ per unit of length [33].

$$P_{\mathrm{cond\,u.l.}} = I^2(\varphi)/2\pi d_{\mathrm{w}}\sigma\delta \tag{21}$$

$$P_{\mathrm{prox\,u.l.}} = \pi d_{\mathrm{w}} H_0^2(\varphi)/\sigma\delta \tag{22}$$

where σ is the electrical conductivity, $\delta = 1/\sqrt{\pi\mu_0\sigma f}$ is the skin depth at the working frequency f and H_0 is the amplitude of external magnetic field applied on the conductor form other wires, which can be calculated by Biot-Savart Law. And parameter $\pi(\varphi)$ is defined as (23). It can be seen that $\pi(\varphi)$ is decided by the coil structure and current distribution.

$$\Pi(\varphi) = H_0(\varphi)/I(\varphi) \tag{23}$$

Thus, the ac resistance $R_{\mathrm{ac\ u.l.}}$ per unit of length is the sum of conduct resistance $R_{\mathrm{cond\ u.l.}}$ and proximity resistance $R_{\mathrm{prox\ u.l.}}$ and can be given by

$$R_{\mathrm{ac\,u.l.}} = R_{\mathrm{cond\,u.l.}} + R_{\mathrm{prox\,u.l.}} = \frac{1}{\pi d_{\mathrm{w}}\sigma\delta} + \frac{2\pi d_{\mathrm{w}}}{\sigma\delta}\Pi^2(\varphi) \tag{24}$$

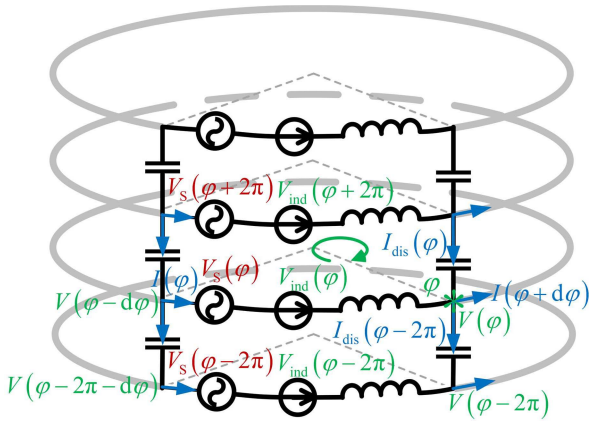

Fig. 11. Distribution of parasitic parameters on a helical coil.

C. Partial-Element Equivalent Circuit

At high frequency, the current distribution along the coil is no longer identical. To obtain an accurate model at high frequency, a small circular segment $[\varphi - \mathrm{d}\varphi, \varphi]$ is separated from the coil with an angle $\mathrm{d}\varphi$. As shown in Fig. 11, the segment $[\varphi - \mathrm{d}\varphi, \varphi]$ begins at node $\varphi - \mathrm{d}\varphi$ and ends at node φ, whose neighbors are segment $[\varphi - \mathrm{d}\varphi - 2\pi, \varphi - 2\pi]$ and segment $[\varphi - \mathrm{d}\varphi + 2\pi, \varphi + 2\pi]$. The self-inductance of segment $[\varphi - \mathrm{d}\varphi, \varphi]$ is $\bar{L}_{\varphi}\mathrm{d}\varphi$ and the mutual inductance between segment $[\varphi - \mathrm{d}\varphi, \varphi]$ and $[\phi - \mathrm{d}\phi, \phi]$ is $\bar{M}_{\varphi\varphi}\mathrm{d}\varphi$. The capacitance between segment $[\varphi - \mathrm{d}\varphi, \varphi]$ and $[\varphi + (j-i)2\pi - \mathrm{d}\varphi, \varphi + (j-i)2\pi]$ is $\bar{C}_{ij}\mathrm{d}\varphi$, where $i = \mathrm{ceil}(\varphi/2\pi)$ and the function ceil represents rounding up.

There is a current $I(\varphi)$ flowing into the segment $[\varphi - \mathrm{d}\varphi, \varphi]$ and a current $I(\varphi + \mathrm{d}\varphi)$ flowing out of it. Furthermore, there is a displacement current $I_{\mathrm{dis}}(\varphi)$ and $I_{\mathrm{dis}}(\varphi - 2\pi)$ flowing into and out of segment $[\varphi - \mathrm{d}\varphi, \varphi]$, respectively. The displacement current is produced by the distributed capacitances and can be calculated by (25), where $V(\varphi)$ represents the voltage at node φ.

$$\begin{aligned} I_{\mathrm{dis}}(\varphi) &= \sum_{j=i+1}^{N} j\omega\bar{C}_{ij}\mathrm{d}\varphi\,[V(\phi) - V(\varphi)] \\ I_{\mathrm{dis}}(\varphi - 2\pi) &= \sum_{j=1}^{i-1} j\omega\bar{C}_{ij}\mathrm{d}\varphi\,[V(\varphi) - V(\phi)] \end{aligned} \tag{25}$$

Appling Kirchhoff's current law to node φ, (26) is obtained.

$$I(\varphi) + I_{\mathrm{dis}}(\varphi) - I(\varphi + d\varphi) - I_{\mathrm{dis}}(\varphi - 2\pi) = 0 \tag{26}$$

Bringing (25) into (26), a new equation can be obtained as follows:

$$\frac{I(\varphi + \mathrm{d}\varphi) - I(\varphi)}{\mathrm{d}\varphi} = \sum_{j=1, j\neq i}^{N} j\omega\bar{C}_{ij}V(\phi) - \sum_{j=1, j\neq i}^{N} j\omega\bar{C}_{ij}V(\varphi) \tag{27}$$

There is a lumped voltage source $V_{\mathrm{S}}(\varphi)$ and an induction voltage source $V_{\mathrm{ind}}(\varphi)$ excited by other coils applied on segment $[\varphi - \mathrm{d}\varphi, \varphi]$. The induced voltage generated by the self inductance of segment $[\varphi - \mathrm{d}\varphi, \varphi]$ is $j\omega L_{\varphi} I(\varphi)$. And

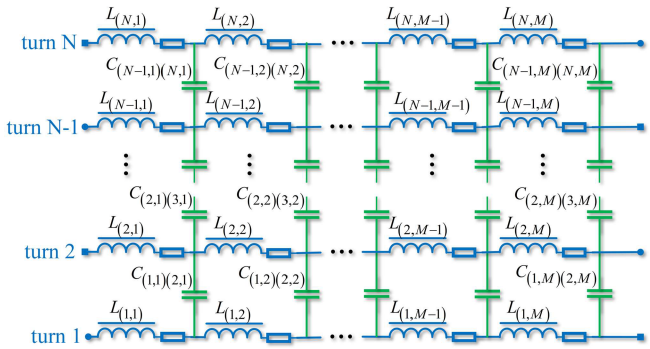

Fig. 12. Partial-element equivalent circuit of a helical coil with N turns and each turn divided into W equal segments.

$\int j\omega\bar{M}_{\varphi\phi}I(\phi)\mathrm{d}\phi$ is the induced voltage generated by other segments of this coil on segment $[\varphi-\mathrm{d}\varphi,\varphi]$. The parasitic resistance of segment $[\varphi-\mathrm{d}\varphi,\varphi]$ plus the load resistance connected to it is donated as R_φ and the voltage drop generated by resistance R_φ is $R_\varphi I(\varphi)$. Appling Kirchhoff's voltage law, the voltage drop between node $\varphi-\mathrm{d}\varphi$ and φ can be written as

$$\begin{aligned} &V(\varphi-d\varphi)-V(\varphi)\\ &=j\omega L_\varphi I(\varphi)+\int j\omega\bar{M}_{\varphi\phi}I(\phi)\mathrm{d}\phi+R_\varphi I(\varphi)+V_{\mathrm{ind}}(\varphi)\\ &\quad -V_{\mathrm{S}}(\varphi) \end{aligned} \tag{28}$$

The above equation can be written as follows:

$$\begin{aligned} &[V(\varphi)-V(\varphi-\mathrm{d}\varphi)]/\mathrm{d}\varphi=-j\omega\bar{L}_\varphi I(\varphi)-j\omega\bar{M}_{\varphi\phi}I(\phi)\\ &\quad-\frac{R_\varphi I(\varphi)}{\mathrm{d}\varphi}+\frac{V_{\mathrm{S}}(\varphi)-V_{\mathrm{ind}}(\varphi)}{\mathrm{d}\varphi} \end{aligned} \tag{29}$$

In order to solve the differential (27) and (29), a numerical difference method is used. Dividing each turn into W equal segments with an angle $\Delta\varphi=2\pi/W$, a PEEC model of helical coil is got as shown in Fig. 12.

The segment w on turn i is regarded as segment (i,w). The mutual inductance between segment (i,w) and (j,s) is denoted as $M_{(i,w),(j,s)}$ and there is $M_{(i,w),(j,s)}=\bar{M}_{(i,w),(j,s)}\,\Delta\varphi$. And the self-inductance of segment (i,w) is denoted as $L_{(i,w)}$ and there is $L_{(i,w)}=\bar{L}_{(i,w)}\,\Delta\varphi$. $\bar{M}_{(i,w),(j,s)}=\bar{M}_{\varphi\phi}$ and $\bar{L}_{(i,w)}=\bar{L}_\varphi$ can be calculated by (11) and (12), where $\varphi=[(i-1)W+w]\,\Delta\varphi$ and $\phi=[(j-1)W+s]\,\Delta\varphi$. The capacitance between segment (i,w) and (j,w) is denoted as $C_{(i,w),(j,w)}=\bar{C}_{(i,w),(j,w)}\,\Delta\varphi$, where $\bar{C}_{(i,w),(j,w)}=\bar{C}_{ij}$ can be calculated by (20).

A row vector is defined in (30) to describe the current flowing on each segment. The voltage on each node can be expressed by (31). And the lumped voltage source and induction voltage excited by other coils applied on each segment can be expressed by (32) and (33), respectively.

$$\mathbf{I}=\left[\begin{array}{ccccc} I_{(1,1)}\cdots I_{(1,W)} & \cdots & I_{(N,1)}\cdots I_{(N,W)}\end{array}\right]^{\mathrm{T}} \tag{30}$$

$$\mathbf{V}=\left[\begin{array}{ccccc} V_{(1,1)}\cdots V_{(1,W)} & \cdots & V_{(N,1)}\cdots V_{(N,W)}\end{array}\right]^{\mathrm{T}} \tag{31}$$

$$\mathbf{V}_{\mathrm{S}}=\left[\begin{array}{ccccc} V_{\mathrm{S}(1,1)}\cdots V_{\mathrm{S}(1,W)} & \cdots & V_{\mathrm{S}(N,1)}\cdots V_{\mathrm{S}(N,W)}\end{array}\right]^{\mathrm{T}} \tag{32}$$

$$\mathbf{V}_{\mathrm{ind}}=\left[V_{\mathrm{ind}(1,1)}\cdots V_{\mathrm{ind}(1,W)}\cdots V_{\mathrm{ind}(N,1)}\cdots V_{\mathrm{ind}(N,W)}\right]^{\mathrm{T}} \tag{33}$$

Thus, (27) can be written in the form of a difference equation.

$$\mathbf{D}_{\mathrm{I}}\mathrm{I}+\mathbf{I}_{\mathrm{B}}/\Delta\varphi=j\omega\widehat{\mathbf{C}}\mathbf{V} \tag{34}$$

where $\mathbf{I}_{\mathrm{B}}=[0\quad 0\cdots I_{(N+11)}]^{\mathrm{T}}$ represents the boundary condition of the current distribution I. There is $I_{(N+11)}=I_{(11)}$ when it's a short-end coil and $I_{(N+11)}=0$ when it's an open-end coil. Thus, $\mathbf{I}_{\mathrm{B}}$ can be written as $\mathbf{I}_{\mathrm{B}}/\Delta\varphi=\mathbf{B}_{\mathrm{I}}\,\mathrm{I}$ and $\mathbf{B}_{\mathrm{I}}$ is the boundary matrix of order NW by NW.

$$\mathbf{B}_{\mathrm{I}}=\begin{cases}\dfrac{1}{\Delta\varphi}\begin{bmatrix}0&0&&0\\0&0&&0\\&&\ddots&\\1&0&&0\end{bmatrix} & \text{short–end}\\ \mathrm{O} & \text{open–end}\end{cases} \tag{35}$$

$\mathbf{D}_{\mathrm{I}}$ is the difference matrix of order NW by NW.

$$\mathbf{D}_{\mathrm{I}}=\frac{1}{\Delta\varphi}\begin{bmatrix}-1&1&&0&0\\0&-1&&0&0\\&&\ddots&&\\0&0&&-1&1\\0&0&&0&-1\end{bmatrix} \tag{36}$$

$\widehat{\mathbf{C}}$ is a matrix of order NW by NW, and the element $\widehat{C}_{xy}$ in the matrix $\widehat{\mathbf{C}}$ is

$$\widehat{C}_{xy}=\begin{cases}-\sum_{k=1,k\neq i}^{N}\bar{C}_{(i,w)(k,w)} & y=x\\ \bar{C}_{(i,w)(j,w)} & y\neq x, y=(j-1)W+w\\ 0 & \text{others}\end{cases} \tag{37}$$

where $i=\mathrm{ceil}(x/W)$, $w=\mathrm{mod}(x/W)$, the function ceil represents rounding up and the function mod represents taking the remainder. Therefore, (34) can be written as

$$(\mathbf{D}_{\mathrm{I}}+\mathbf{B}_{\mathrm{I}})\,\mathbf{I}=\mathbf{j}\omega\widehat{\mathbf{C}}\mathbf{V} \tag{38}$$

Similarly, (29) can be written into a difference equation.

$$\mathbf{D}_{\mathrm{V}}\mathbf{V}=-\mathbf{j}\omega\widehat{\mathbf{M}}\mathbf{I}-\widehat{\mathbf{R}}\mathbf{I}+(\mathbf{V}_{\mathrm{S}}-\mathbf{V}_{\mathrm{ind}})/\boldsymbol{\Delta}\varphi \tag{39}$$

where $\mathbf{D}_{\mathrm{V}}$ is the difference matrix of order NW by NW.

$$\mathbf{D}_{\mathrm{V}}=\frac{1}{\Delta\varphi}\begin{bmatrix}1&0&&0&0\\-1&1&&0&0\\&&\ddots&&\\0&0&&1&0\\0&0&&-1&1\end{bmatrix} \tag{40}$$

$\widehat{\mathbf{M}}$ is a matrix of order NW by NW, and the element $\widehat{M}_{xy}$ in the matrix $\widehat{\mathbf{M}}$ is

$$\widehat{M}_{xy}=\begin{cases}\bar{L}_{(i,w)} & y=x\\ \bar{M}_{(i,w)(j,s)} & y\neq x\end{cases} \tag{41}$$

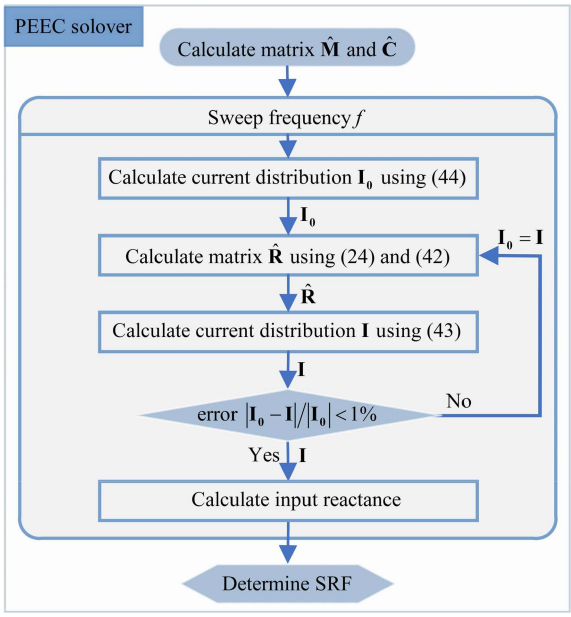

Fig. 13. Algorithm flow chart of the PEEC solver.

where $i = \text{ceil}(x/W)$, $m = \text{mod}(x/W)$ and $j = \text{ceil}(y/W)$, $s = \text{mod}(y/W)$. $\widehat{\mathbf{R}}$ is a matrix of order NW by NW, and the element $\widehat{R}_{xy}$ in the matrix $\widehat{\mathbf{R}}$ is

$$\widehat{R}_{xy} = \begin{cases} r_{\mathrm{H}} R_{\mathrm{ac\,u.l.}x} + R_{\mathrm{L}x}/\Delta\varphi & y = x \\ 0 & y \neq x \end{cases} \tag{42}$$

Combining (38) and (39), we can get the expression about the current distribution I.

$$\mathbf{I} = \frac{\mathbf{1}}{\boldsymbol{\Delta\varphi}} \left[\mathbf{D}_{\mathrm{V}} \left(\mathbf{j}\omega \widehat{\mathbf{C}} \right)^{-\mathbf{1}} (\mathbf{D}_{\mathrm{I}} + \mathbf{B}_{\mathrm{I}}) + \mathbf{j}\omega \widehat{\mathbf{M}} + \widehat{\mathbf{R}} \right]^{-\mathbf{1}} (\mathbf{V}_{\mathrm{S}} - \mathbf{V}_{\mathrm{ind}}) \tag{43}$$

However, the parasitic resistance is affected by the current distribution, so equation (43) cannot be solved directly. Neglecting the parasitic resistance, the above equation can be written as (44) and an initial current distribution $\mathbf{I_0}$ can be solved directly.

$$\mathbf{I}_0 = \frac{1}{\Delta\varphi} \left[\mathbf{D}_{\mathrm{V}} \left(j\omega \widehat{\mathbf{C}} \right)^{-1} (\mathbf{D}_{\mathrm{I}} + \mathbf{B}_{\mathrm{I}}) + j\omega \widehat{\mathbf{M}} \right]^{-1} \mathbf{V}_{\mathrm{S}} \tag{44}$$

Based on the above analysis, a MATLAB program called PEEC solver is written to calculate the SRFs and the current distributions. Fig. 13 is the algorithm flow chart. First, the matrix $\widehat{\mathbf{M}}$ and $\widehat{\mathbf{C}}$ are calculated for a given helical coil. Then, an initial current distribution $\mathbf{I_0}$ is obtained using (44). Utilizing the current distribution $\mathbf{I_0}$, the parasitic resistance $\widehat{\mathbf{R}}$ can be obtained. The current distribution I is recalculated utilizing (43) considering the parasitic resistance $\widehat{\mathbf{R}}$. Iterating this process, the new current distribution I and parasitic resistance $\widehat{\mathbf{R}}$ can be obtained. When the iteration error is less than 1%, the obtained current distribution I is used as the final result. The input impedance can be calculated by dividing the source voltage by the current on the source. As analyzed in part A of Section III,

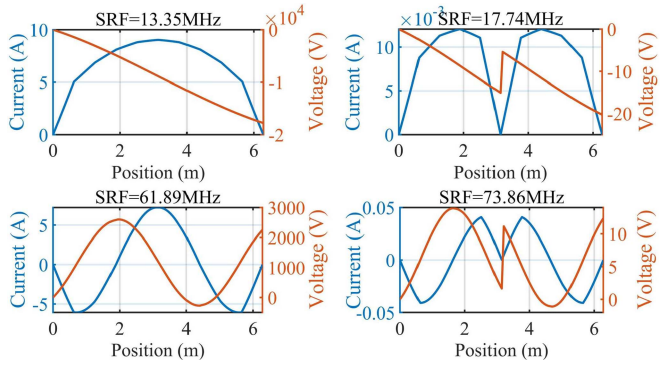

Fig. 14. The current distribution (blue line) and voltage distribution (orange line) along the coil at the first four SRFs.

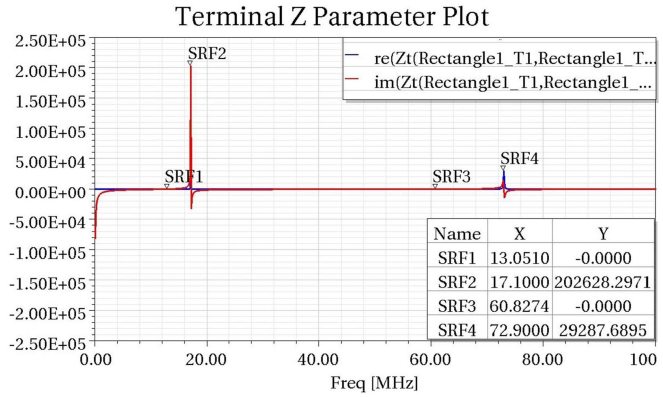

Fig. 15. Terminal impedance versus frequency simulated by ANSYS HFSS.

the input reactance is zero or infinite when the coil resonates. The value of SRF can be obtained by sweeping frequency.

Taking an open-end Archimedean helix as an example, its radius r_{H} is 100 mm, its pitch p is 4 mm, and it has 10 turns. The diameter d_{w} of wire is 2 mm. There is a 10 V lumped voltage source applied on the middle segment of the coil. Each turn is divided into 10 equal segments. Fig. 14 shows the current and voltage distribution along the coil at the first four SRFs calculated by PEEC solver. It can be seen from Fig. 14 that the first four SRFs of the open-end Archimedean helix are 13.35, 17.74, 61.89, and 73.86 MHz, respectively. The current distribution along the coil is a standing wave, but not a standard sinusoidal wave. At 1st SRF and 3rd SRF, the currents reached the maximum in input port, showing the characteristic of LC series resonance. At 2nd SRF and 4th SRF, the currents in the input port are zero, showing the characteristic of LC parallel resonance.

To verify the correctness of PEEC model, the above helical coil was simulated by ANSYS HFSS, a 3D electromagnetic (EM) simulation tool. On an Intel Xeon 6258R processor (basic frequency 3.3 GHz), the frequency is swept from 100 kHz to 100 MHz, scanning 1000 points uniformly. The PEEC solution process takes 21.745 seconds, while HFSS takes 5.05 hours which is 836 times that of PEEC solver. Fast computation is of great help to the rapid design of self-resonant coils. Fig. 15 shows the terminal impedance varies with frequency. And the

TABLE I
COMPARISON OF THE PEEC CALCULATION, HFSS SIMULATION AND VNA MEASUREMENT RESULTS OF SRFS

No.		Calculation SRF /MHz	Simulation SRF /MHz	Simulation error	Measurement SRF /MHz	Measurement error
Coil1	1st SF	13.35	13.05	2.45%	12.84	3.97%
	1st PF	17.74	17.10	3.74%	16.23	9.30%
	2nd SF	61.89	60.83	1.74%	58.68	5.47%
	2nd PF	73.86	72.90	1.32%	67.83	8.89%
Coil2	1st SF	21.46	21.47	0.05%	21.11	1.66%
	1st PF	27.83	27.20	2.32%	25.35	9.78%
	2nd SF	77.98	76.63	1.64%	75.06	3.89%
	2nd PF	89.60	87.91	1.92%	81.67	9.71%
Coil3	1st SF	9.11	9.03	0.89%	8.97	1.56%
	1st PF	12.59	12.44	1.21%	11.52	9.28%
	2nd SF	41.87	41.45	1.01%	40.39	3.66%
	2nd PF	51.02	50.67	0.69%	46.66	9.34%

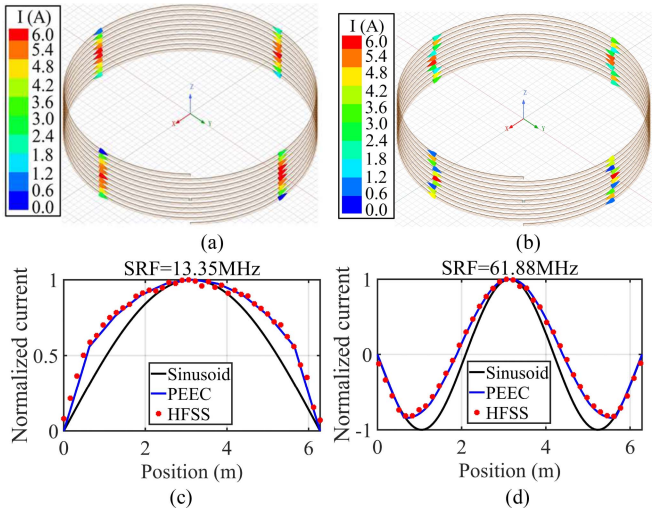

Fig. 16. Current distribution in 3D coordinate at (a) 1st SF (b) 2nd SF. Normalized current distribution curves along the coil at (c) 1st SF (d) 2nd SF.

first four SRFs simulated by HFSS are 13.05, 17.10, 60.83, and 72.90 MHz, respectively. It can be seen that the SRFs calculated by PEEC are in good agreement with values simulated by HFSS, and the maximum error is no more than 4%. However, the first four SRFs calculated by transmission line model are 23.87, 47.74, 71.62, and 95.49 MHz, which have large errors compared with simulation results.

The helical coil was fabricated and measured with vector network analyzer (VNA). In addition, two other helical coils with different structural parameters were fabricated, whose radius r_{H} are 50 and 150 mm, pitch p are 4 and 6 mm, and turn number are 16 and 10, respectively. And the diameter d_{w} of wire is 2 mm. The SRFs are shown and compared in Table I. The errors between the PEEC calculation results and the HFSS simulation values do not exceed 4%. And the errors relative to VNA measurement values do not exceed 10%.

To record the current distribution, a series of observation points are set along the coil. And the current distributions at 1st SF and 2nd SF are shown in Fig. 16(a) and (b) in 3D coordinate respectively, where the amplitude of current is represented by the colormap. The normalized current distribution curves along

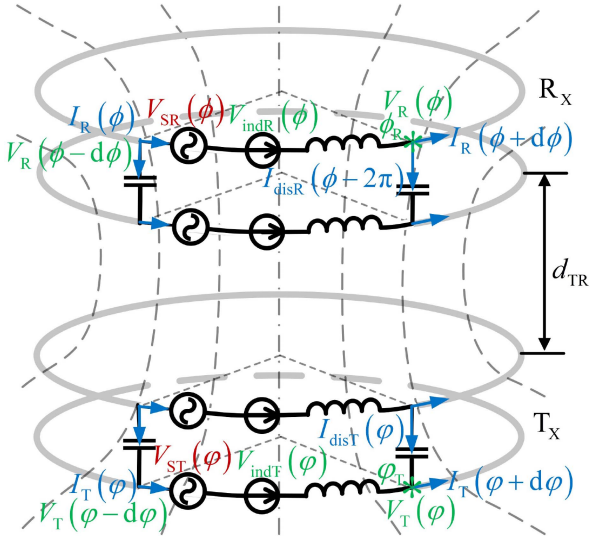

Fig. 17. Distribution of parasitic parameters on two coupled helical coils.

the observation points are shown in Fig. 16(c) and (d). For comparison, the sinusoidal curves of transmission line model and the normalized current distribution curves calculated by PEEC model are added in Fig. 16(c) and (d). It can be seen that the curves calculated by PEEC are in good agreement with HFSS, but are significantly different from the sinusoidal curves.

The quality factor Q is defined as the ratio of the energy stored E_{M} in the coil to the energy dissipated E_{D} per cycle

$$Q(\omega) = 2\pi E_{\mathrm{M}}/E_{\mathrm{D}} = \omega E_{\mathrm{M}}/P_{\mathrm{loss}} \tag{45}$$

For the self-resonant coil, the magnetic field energy and the power loss can be calculated by $E_{\mathrm{M}} = 1/2\mathbf{I}^{\mathrm{T}}\widehat{\mathbf{M}}\Delta\varphi\mathbf{I}^{*}$ and $P_{\mathrm{loss}} = 1/2\mathbf{I}^{\mathrm{T}}\widehat{\mathbf{R}}\Delta\varphi\mathbf{I}^{*}$, respectively. Therefore, the quality factor Q of self-resonant coil is

$$Q(\omega) = \omega\frac{E_{\mathrm{M}}}{P_{\mathrm{loss}}} = \omega\frac{\mathbf{I}^{\mathrm{T}}\widehat{\mathbf{M}}\mathbf{I}^{*}}{\mathbf{I}^{\mathrm{T}}\widehat{\mathbf{R}}\mathbf{I}^{*}} \tag{46}$$

Using (46), the quality factor Q of coil 1 is 1609 at the first SRF. The quality factor simulated by HFSS is 1472 at the first SRF, indicating the correctness of PEEC model. The quality factor of the traditional coil with a compensation network is generally 50-300. It can be seen that the self-resonant coil has a high quality factor, which has great advantages in high-power level and high-efficiency transmission for mid-range WPT applications.

IV. MODELING OF MAGNETIC COUPLING MECHANISM

Considering of two coupled self-resonant helical coils as shown in Fig. 17, the radius of Tx is r_{T}, the turn number is N_{T}, the turn pitch is p_{T} and the radius of Rx is r_{R}, the turn number is N_{R}, the turn pitch is p_{R}. The distance between Tx and Rx is d_{TR}. The lumped mutual inductance cannot be used to describe the interaction between two coils due to the varying current distribution along the coil. Thus, a PEEC model is built to describe the magnetic coupling mechanism between Tx and Rx.

Consider the segment $[\varphi-\mathrm{d}\varphi,\varphi]$ of Tx and the segment $[\phi-\mathrm{d}\phi,\phi]$ of Rx, the partial mutual inductance can be calculated by

$$\begin{aligned} M_{\mathrm{T}\varphi}^{\mathrm{R}\phi} &= \frac{\mu_0}{4\pi}\iint \frac{\mathrm{d}\boldsymbol{l}_{\mathrm{T}\varphi}\cdot\mathrm{d}\boldsymbol{l}_{\mathrm{R}\phi}}{|\boldsymbol{\rho}_{\mathrm{T}\varphi}-\boldsymbol{\rho}_{\mathrm{R}\phi}|} \\ &= \frac{\mu_0 r_{\mathrm{T}} r_{\mathrm{R}}}{4\pi}\int_{\varphi-\mathrm{d}\varphi}^{\varphi}\int_{\phi-\mathrm{d}\phi}^{\phi} \\ &\quad \frac{\sin\varphi\sin\phi+\cos\varphi\cos\phi}{\sqrt{{r_{\mathrm{T}}}^2+{r_{\mathrm{R}}}^2-2r_{\mathrm{T}}r_{\mathrm{R}}\cos(\varphi-\phi)+z_{\varphi\phi}^2}}\mathrm{d}\phi\mathrm{d}\varphi \\ &= \bar{M}_{\mathrm{T}\varphi}^{\mathrm{R}\phi}\mathrm{d}\varphi \end{aligned} \tag{47}$$

where $z_{\varphi\phi}$ is the vertical distance between segment $[\varphi-\mathrm{d}\varphi,\varphi]$ of Tx and segment $[\phi-\mathrm{d}\phi,\phi]$ of Rx.

The induction voltage $V_{\mathrm{indT}}(\varphi)$ is excited by the current I_{R} of Rx and $V_{\mathrm{indR}}(\phi)$ is excited by the current I_{T} of Tx.

$$V_{\mathrm{indT}}(\varphi) = \int \bar{M}_{\mathrm{R}\phi}^{\mathrm{T}\varphi} I_{\mathrm{R}}(\phi)\,\mathrm{d}\phi \tag{48}$$

$$V_{\mathrm{indR}}(\phi) = \int \bar{M}_{\mathrm{T}\varphi}^{\mathrm{R}\phi} I_{\mathrm{T}}(\varphi)\,\mathrm{d}\varphi \tag{49}$$

In order to solve the differential equation, a numerical difference method is used. Dividing each turn of Tx and Rx into W equal segments with an angle $\Delta\varphi=2\pi/W$ and $\Delta\phi=2\pi/W$, the mutual inductance between segment (i,w) of Tx and segment (j,s) of Rx is $M_{\mathrm{T}(i,w)}^{\mathrm{R}(j,s)}=\bar{M}_{\mathrm{T}(i,w)}^{\mathrm{R}(j,s)}\,\Delta\varphi$, where $\bar{M}_{\mathrm{T}(i,w)}^{\mathrm{R}(j,s)}=\bar{M}_{\mathrm{T}\varphi}^{\mathrm{R}\phi}$ is calculated by (47), $\varphi=[(i-1)W+w]\,\Delta\varphi$ and $\phi=[(j-1)W+s]\,\Delta\varphi$.

The induction voltage in (48) and (49) can be written as

$$V_{\mathrm{indT}(i,w)} = \sum_{j=1}^{N_{\mathrm{R}}}\sum_{s=1}^{W} j\omega\bar{M}_{\mathrm{T}(i,w)}^{\mathrm{R}(j,s)}\Delta\varphi I_{\mathrm{R}(j,s)} \tag{50}$$

$$V_{\mathrm{indR}(j,s)} = \sum_{i=1}^{N_{\mathrm{T}}}\sum_{w=1}^{W} j\omega\bar{M}_{\mathrm{T}(i,w)}^{\mathrm{R}(j,s)}\Delta\varphi I_{\mathrm{T}(i,w)} \tag{51}$$

The above equation can be written in matrix form.

$$\mathbf{V}_{\mathrm{indT}} = j\omega\widehat{\mathbf{M}}_{\mathrm{TR}}\Delta\varphi\mathbf{I}_{\mathrm{R}} \tag{52}$$

$$\mathbf{V}_{\mathrm{indR}} = j\omega\widehat{\mathbf{M}}_{\mathrm{RT}}\Delta\varphi\mathbf{I}_{\mathrm{T}} \tag{53}$$

where $\widehat{\mathbf{M}}_{\mathrm{TR}}$ is a matrix of order $N_{\mathrm{R}}W$ by $N_{\mathrm{T}}W$, and $\widehat{\mathbf{M}}_{\mathrm{RT}}=\widehat{\mathbf{M}}_{\mathrm{TR}}^{\mathrm{T}}$. The element $\widehat{M}_{\mathrm{TR}xy}$ in matrix $\widehat{\mathbf{M}}_{\mathrm{TR}}$ is

$$\widehat{M}_{\mathrm{TR}xy} = \bar{M}_{\mathrm{T}(i,w)}^{\mathrm{R}(j,s)} \quad x=(j-1)W+s, y=(i-1)W+w \tag{54}$$

For Tx, (38) and (39) can be written as

$$\begin{cases} (\mathbf{D}_{\mathrm{IT}}+\mathbf{B}_{\mathrm{IT}})\mathbf{I}_{\mathrm{T}} = j\omega\widehat{\mathbf{C}}_{\mathrm{T}}\mathbf{V}_{\mathrm{T}} \\ \mathbf{D}_{\mathrm{VT}}\mathbf{V}_{\mathrm{T}} = -j\omega\widehat{\mathbf{M}}_{\mathrm{T}}\mathbf{I}_{\mathrm{T}} - \widehat{\mathbf{R}}_{\mathrm{T}}\mathbf{I}_{\mathrm{T}} + (\mathbf{V}_{\mathrm{ST}}-\mathbf{V}_{\mathrm{indT}})/\Delta\varphi \end{cases} \tag{55}$$

From above equations, we can get (56) about the current distribution $\mathbf{I}_{\mathrm{T}}$ and the matrix $\mathbf{G}_{\mathrm{T}}$ is defined as the feature matrix of Tx.

$$\begin{aligned} \mathbf{I}_{\mathrm{T}} &= \frac{1}{\Delta\varphi}\left[\mathbf{D}_{\mathrm{VT}}\left(j\omega\widehat{\mathbf{C}}_{\mathrm{T}}\right)^{-1}(\mathbf{D}_{\mathrm{IT}}+\mathbf{B}_{\mathrm{IT}})+j\omega\widehat{\mathbf{M}}_{\mathrm{T}}+\widehat{\mathbf{R}}_{\mathrm{T}}\right]^{-1} \\ &\quad (\mathbf{V}_{\mathrm{ST}}-\mathbf{V}_{\mathrm{indT}}) \\ &= \mathbf{G}_{\mathrm{T}}(\mathbf{V}_{\mathrm{ST}}-\mathbf{V}_{\mathrm{indT}})/\Delta\varphi \end{aligned} \tag{56}$$

Combining with (52), the current $\mathbf{I}_{\mathrm{T}}$ can be written as

$$\mathbf{I}_{\mathrm{T}} = \mathbf{G}_{\mathrm{T}}\mathbf{V}_{\mathrm{ST}}/\Delta\varphi - j\omega\mathbf{G}_{\mathrm{T}}\widehat{\mathbf{M}}_{\mathrm{TR}}\mathbf{I}_{\mathrm{R}} \tag{57}$$

For Rx, (38) and (39) can be written as

$$\begin{cases} (\mathbf{D}_{\mathrm{IR}}+\mathbf{B}_{\mathrm{IR}})\mathbf{I}_{\mathrm{R}} = j\omega\widehat{\mathbf{C}}_{\mathrm{R}}\mathbf{V}_{\mathrm{R}} \\ \mathbf{D}_{\mathrm{VR}}\mathbf{V}_{\mathrm{R}} = -j\omega\widehat{\mathbf{M}}_{\mathrm{R}}\mathbf{I}_{\mathrm{R}} - \widehat{\mathbf{R}}_{\mathrm{R}}\mathbf{I}_{\mathrm{R}} - \mathbf{V}_{\mathrm{indR}}/\Delta\varphi \end{cases} \tag{58}$$

It is worth noting that the element $\widehat{R}_{Rzz}$ in the matrix $\widehat{\mathbf{R}}_{\mathrm{R}}$ is increased by $R_{\mathrm{L}}/\Delta\varphi$ as shown in (42) when the load resistance R_{L} is connected to the segment z of Rx.

From above equations, we can get (59) about the current distribution $\mathbf{I}_{\mathrm{R}}$ and the matrix $\mathbf{G}_{\mathrm{R}}$ is defined as the feature matrix of Rx.

$$\begin{aligned} \mathbf{I}_{\mathrm{R}} &= \frac{-1}{\Delta\varphi}\left[\mathbf{D}_{\mathrm{VR}}\left(j\omega\widehat{\mathbf{C}}_{\mathrm{R}}\right)^{-1}(\mathbf{D}_{\mathrm{IR}}+\mathbf{B}_{\mathrm{IR}})+j\omega\widehat{\mathbf{M}}_{\mathrm{R}}+\widehat{\mathbf{R}}_{\mathrm{R}}\right]^{-1} \\ &\quad \mathbf{V}_{\mathrm{indR}} \\ &= -\mathbf{G}_{\mathrm{R}}\mathbf{V}_{\mathrm{indR}}/\Delta\varphi \end{aligned} \tag{59}$$

Combining with (53), the current $\mathbf{I}_{\mathrm{R}}$ can be written as

$$\mathbf{I}_{\mathrm{R}} = -j\omega\mathbf{G}_{\mathrm{R}}\widehat{\mathbf{M}}_{\mathrm{RT}}\mathbf{I}_{\mathrm{T}} \tag{60}$$

Combining (57) and (60), we obtain (61). It can be seen that (61) has the same form as the standard coupled circuit (1). Therefore, (61) can be easily understood. $\widehat{\mathbf{M}}_{\mathrm{TR}}$ and $\widehat{\mathbf{M}}_{\mathrm{RT}}$ represent the mutual inductance matrix between Tx and Rx. $\mathrm{G}_{\mathrm{T}}^{-1}$ and $\mathrm{G}_{\mathrm{R}}^{-1}$ are the impedance matrix of Tx and Rx, respectively.

$$\frac{1}{\Delta\varphi}\begin{bmatrix}\mathbf{V}_{\mathrm{ST}}\\ 0\end{bmatrix} = \begin{bmatrix}\mathbf{G}_{\mathrm{T}}^{-1} & j\omega\widehat{\mathbf{M}}_{\mathrm{TR}}\\ j\omega\widehat{\mathbf{M}}_{\mathrm{RT}} & \mathbf{G}_{\mathrm{R}}^{-1}\end{bmatrix}\begin{bmatrix}\mathbf{I}_{\mathrm{T}}\\ \mathbf{I}_{\mathrm{R}}\end{bmatrix} \tag{61}$$

The current distribution $\mathbf{I}_{\mathrm{T}}$ and $\mathbf{I}_{\mathrm{R}}$ from (61) and can be calculated by

$$\begin{cases} \mathbf{I}_{\mathrm{T}} = \left(\mathbf{P}+\omega^2\mathbf{G}_{\mathrm{T}}\widehat{\mathbf{M}}_{\mathrm{TR}}\mathbf{G}_{\mathrm{R}}\widehat{\mathbf{M}}_{\mathrm{RT}}\right)^{-1}\mathbf{G}_{\mathrm{T}}\mathbf{V}_{\mathrm{ST}}\Big/\Delta\varphi \\ \mathbf{I}_{\mathrm{R}} = -j\omega\mathbf{G}_{\mathrm{R}}\widehat{\mathbf{M}}_{\mathrm{RT}}\mathbf{I}_{\mathrm{T}} \end{cases} \tag{62}$$

Tx and Rx are the same open-end Archimedean helical coils mentioned in Section III, whose radius r_{H} is 100 mm, pitch p_{H} is 4 mm, and turn number N is 10. The diameter d_{w} of wire is 2 mm. There is a 10 V lumped voltage source applied on the middle segment of Tx. And a 10 Ω load resistance is connected to the middle segment of Rx. The distance between Tx and Rx is 200 mm. Fig. 18(a) shows the current distribution curves along Tx and Rx at the first SRF calculated by PEEC. The current distributions are also simulated by HFSS. In Fig. 18(b), the current distributions are displayed in 3D coordinate, where the amplitude of current is represented by the colormap.

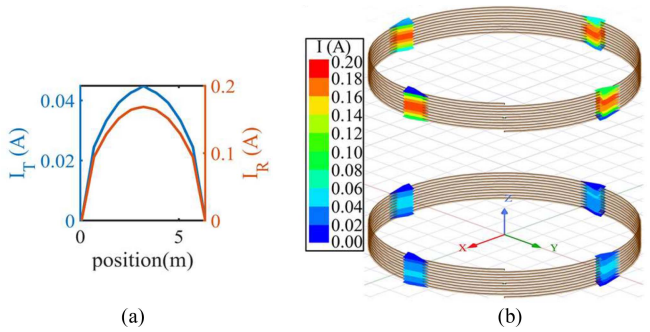

Fig. 18. (a) Current distribution curves of Tx and Rx calculated by PEEC at the first SRF. (b) Current distributions of Tx and Rx displayed in 3D coordinate simulated by HFSS at the first SRF.

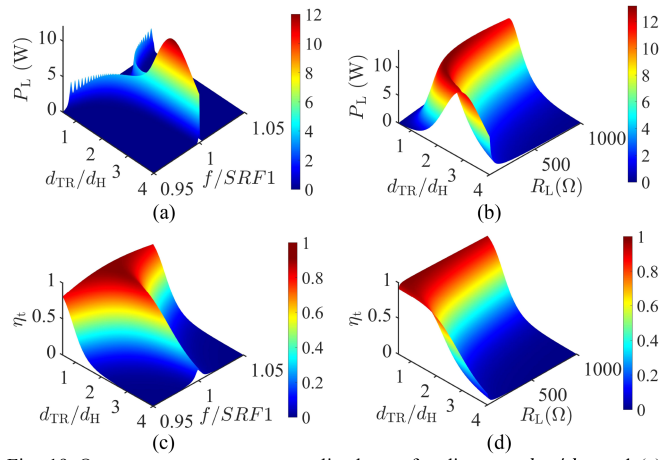

Fig. 19. Output power versus normalized transfer distance $d_{\mathrm{TR}}/d_{\mathrm{H}}$ and (a) normalized frequency $f/SRF1$ (when $R_{\mathrm{L}} = 10\,\Omega$) (b) load resistance R_{L} (when $f/SRF1 = 1$). Transfer efficiency η_{t} versus normalized transfer distance $d_{\mathrm{TR}}/d_{\mathrm{H}}$ for and (c) normalized frequency $f/SRF1$ (when $R_{\mathrm{L}} = 10\,\Omega$) (d) load resistance R_{L} (when $f/SRF1 = 1$).

Because the voltage source and load resistance are connected to the middle segment of Tx and Rx respectively, there are $I_{\mathrm{S}} = \mathbf{I}_{\mathrm{Tmid}}$ and $I_{\mathrm{L}} = \mathbf{I}_{\mathrm{Rmid}}$. The subscript mid indicates the value on the middle segment of the row vector. The output power can be calculated by $P_{\mathrm{L}} = \mathbf{I}^{\mathbf{2}}_{\mathrm{Tmid}}\,\mathbf{R}_{\mathrm{L}}$, and the transfer efficiency can be calculated by $\eta_{\mathrm{t}} = \mathbf{I}^{\mathbf{2}}_{\mathrm{Tmid}}\,\mathbf{R}_{\mathrm{L}}/\mathrm{Re}[\mathbf{V}_{\mathrm{S}}\mathbf{I}_{\mathrm{Tmid}}]$. Fig. 19(a) and (c) shows the output power P_{L} and transfer efficiency η_{t} versus the normalized transfer distance $d_{\mathrm{TR}}/d_{\mathrm{H}}$ and the normalized frequency $f/SRF1$ when $R_{\mathrm{L}} = 10\,\Omega$, respectively. $SRF1$ is the value of the first SRF. As discussed in Section II, when the Tx and Rx are in close coupling, the frequency splitting phenomenon occurs that the output power is maximum at the two splitting frequencies. When the two coils are in loose coupling, the output power reaches its maximum value at the SRF. Fig. 19(b) and (d) show the output power P_{L} and transfer efficiency η_{t} versus the normalized transfer distance $d_{\mathrm{TR}}/d_{\mathrm{H}}$ and load resistance R_{L} when $f/SRF1 = 1$, respectively. Different transfer distances correspond to different load resistance to maximize the output power P_{L}.

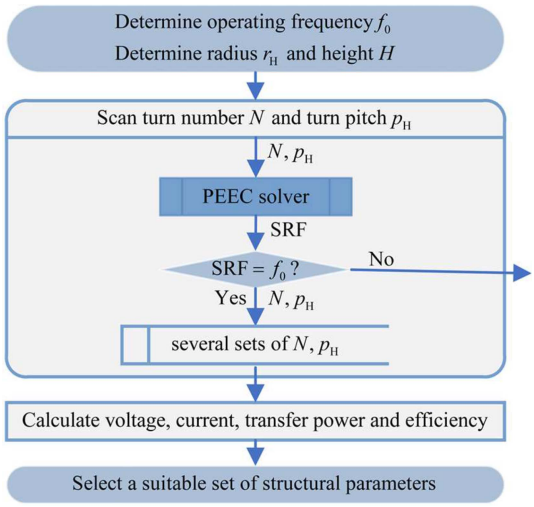

Fig. 20. Flow chart of design guideline for self-resonant coils.

V. Design Guidelines and Demonstration

A. Design Guideline

In the previous sections, we built a PEEC model of helical coils. The SRF is decided by the coil's parameters and can be calculated by the PEEC solver. The magnetic coupling mechanism between Tx and Rx is also modeled by PEEC. The output power P_{L} and the transfer efficiency η_{t} are obtained. A suitable set of parameters can be selected to meet the requirements of the application. The design guideline for self-resonant helical coils is as follows and the flow chart of design guideline is shown in Fig. 20.

1) Determine the operating frequency

Generally, the operating frequency f_0 is restricted by laws, regulations and standards. Therefore, we need to choose an appropriate SRF within these frequency ranges.

2) Determine the outer dimensions of the coil

In practical applications, there are restrictions on the size of Tx and Rx. The radius r_{H} and height H of the helical coil are usually required to not exceed the limit values.

3) Design the turn number and turn pitch

With the limitation of radius and height, the SRF of the helix is decided by the turn number N and the turn pitch p. Scanning the value of N and p_{H}, the SRF is adjust to the predefined value f_0. Generally, there are several sets of N and p_{H} that satisfy the SRF condition.

4) Calculate voltage, current, transfer power and efficiency

Using the PEEC model of magnetic coupling mechanism, the voltage, current, transfer power and efficiency can be calculated based on different structural parameters. We can select a suitable set of structural parameters that meets the requirements of the application.

B. Fabrication and Measurement

In order to meet the Alliance for Wireless Power (A4WP) standard, the operating frequency f_0 is selected at 6.78 MHz. The radius r_{H} of the coil is set at 150 mm, and the height H of

TABLE II
TURN NUMBER AND THE TURN PITCH OF 6.78 MHZ HELICAL COILS

d_w / N	0.5 mm	1 mm	1.5 mm	2 mm	2.5 mm	3 mm
	p(mm)					
9	0.581	--	--	--	--	--
10	0.924	1.25	--	--	--	--
11	1.44	1.88	2.14	2.35	2.58	--
12	2.23	2.71	3.03	3.15	3.48	3.67
13	3.29	3.80	4.13	4.47	4.63	4.81
14	4.60	5.06	5.38	5.76	5.89	6.15
15	6.03	6.61	--	--	--	--

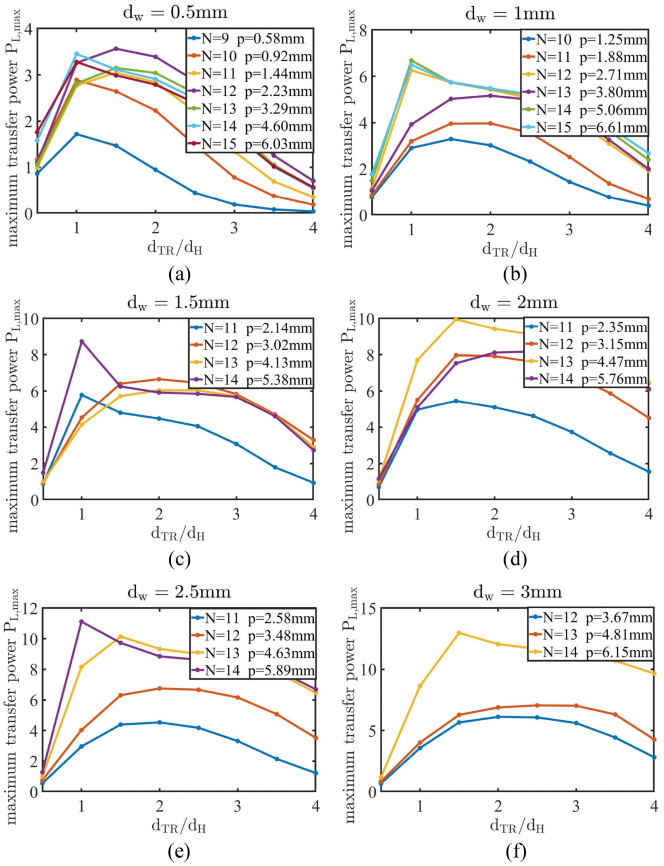

Fig. 21. Maximum transfer power $P_{L,max}$ versus normalized transfer distance d_{TR}/d_H of different 6.78 MHz self-resonant helical coils. The diameter d_w of wire is (a) 0.5 mm (b) 1 mm (c) 1.5 mm (d) 2 mm (e) 2.5 mm (f) 3 mm.

the coil does not exceed 100 mm. Using PEEC solver to scan the structure parameters, several sets of turn number N and turn pitch p_H are obtained to make the SRF of the helical coil reach 6.78 MHz as shown in Table II.

The Tx and Rx are two identical 6.78 MHz self-resonant helical coils and are placed coaxially. Fig. 21 shows the maximum transfer power $P_{L,max}$ versus the normalized transfer distance d_{TR}/d_H. The maximum transfer power first increases and then decreases with the increase of normalized transfer distance. Because when Tx and Rx are close, frequency splitting occurs.

Fig. 22 shows the maximum transfer efficiency $\eta_{t,max}$ versus the normalized transfer distance d_{TR}/d_H. It can be seen that the maximum transfer efficiency decreases with the increase of the normalized transfer distance.

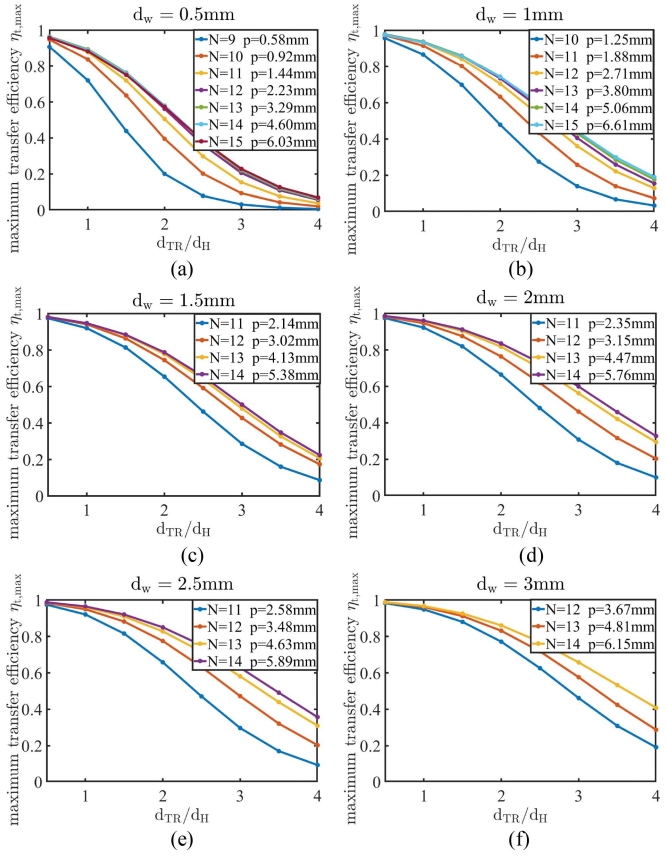

Fig. 22. Maximum transfer efficiency $\eta_{t,max}$ versus normalized transfer distance d_{TR}/d_H of different 6.78 MHz self-resonant helical coils. The diameter d_w of wire is (a) 0.5 mm (b) 1 mm (c) 1.5 mm (d) 2 mm (e) 2.5 mm (f) 3 mm.

When the normalized transfer distance d_{TR}/d_H is between 1 and 3, the coil with $N = 14$, $p = 5.76$ mm and $d_w = 2$ mm has the best performance considering the maximum power transfer principle and maximum transfer efficiency principle. Calculated by PECC, the first SRF of this coil is 6.79 MHz and the quality factor Q is 1805 at 6.79 MHz. The self-resonant helical coil was fabricated and measured as shown in Fig. 23(a). The Tx and Rx are connected to port 1 and port 2 of VNA via 50 Ω coaxial lines, respectively. The measured SRF is 6.68 MHz, which is in good agreement with the calculated result.

The S-parameters between Tx and Rx versus frequency are shown in Fig. 23(b)–(e) at different normalized transfer distance d_{TR}/d_H. S_{11} and S_{22} is the input reflection coefficient and the output reflection coefficient, respectively. S_{12} is the reverse transmission coefficient and S_{21} is the forward transmission coefficient. $|S_{ij}|^2$ indicates the ratio of the energy output from port j to the energy injected into port i. It can be seen from Fig. 23(b) and (c) that the energy coupled to the output is not the maximum at SRF. This is because the transfer distance is small and the frequency splitting phenomenon occurs. As the transfer distance increases, the frequency splitting phenomenon disappears and the maximum energy is transferred at SRF as shown in Fig. 23(d) and (e).

When the load resistance R_L is 50 Ω, the relationship of the input reflection coefficient S_{11}, the forward transmission

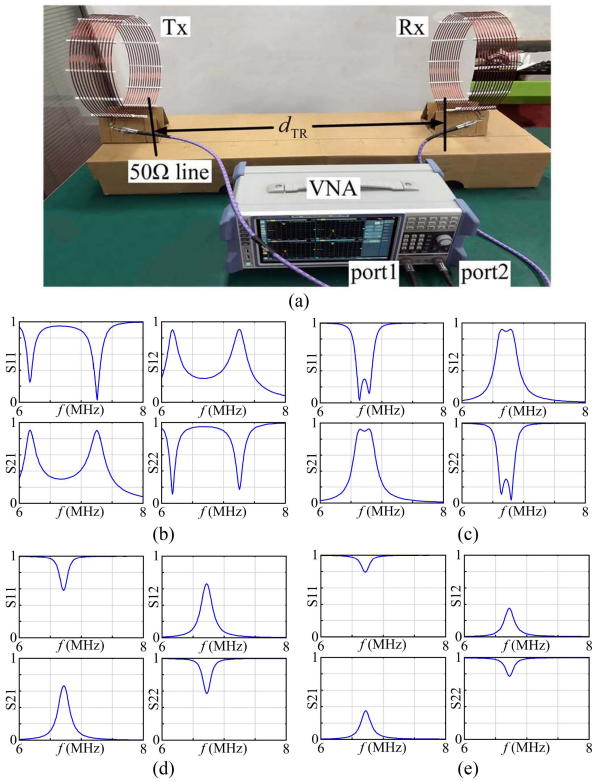

Fig. 23. (a) Photograph of the measurement setup. The diagram of S parameters from 6 to 8 MHz at different normalized transfer distance $d_{\mathrm{TR}}/d_{\mathrm{H}}$. (b) $d_{\mathrm{TR}}/d_{\mathrm{H}} = 1/3$. (c) $d_{\mathrm{TR}}/d_{\mathrm{H}} = 3/3$. (d) $d_{\mathrm{TR}}/d_{\mathrm{H}} = 5/3$. (e) $d_{\mathrm{TR}}/d_{\mathrm{H}} = 7/3$.

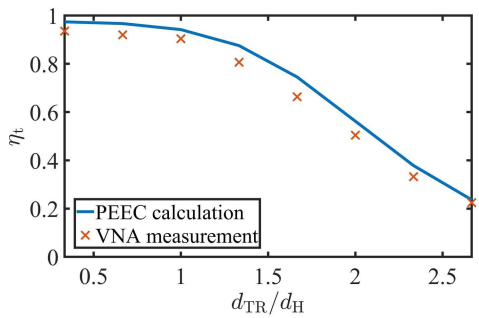

Fig. 24. Transfer efficiency η_t at SRF calculated by PEEC and measured by VNA when the load resistance R_{L} is 50 Ω.

coefficient S_{21} and the coil-to-coil transfer efficiency η_{t} is

$$\eta_{\mathrm{t}} = |S_{21}|^2 \Big/ \left(1 - |S_{11}|^2\right) \tag{63}$$

The transfer efficiency can be calculate theoretically using PEEC model. For comparison, the transfer efficiency is also calculated by (63) using the S-parameters measured by VNA. The relationship between the transfer efficiency η_{t} and the normalized transfer distance $d_{\mathrm{TR}}/d_{\mathrm{H}}$ is shown in Fig. 24.

Good agreement is achieved between the theoretically calculated predications and measurement results. It can be seen that the transfer efficiency η_{t} is about 90% when the normalized transfer distance $d_{\mathrm{TR}}/d_{\mathrm{H}}$ is less than 1. With the increase of transfer distance, the transfer efficiency η_{t} decreases gradually.

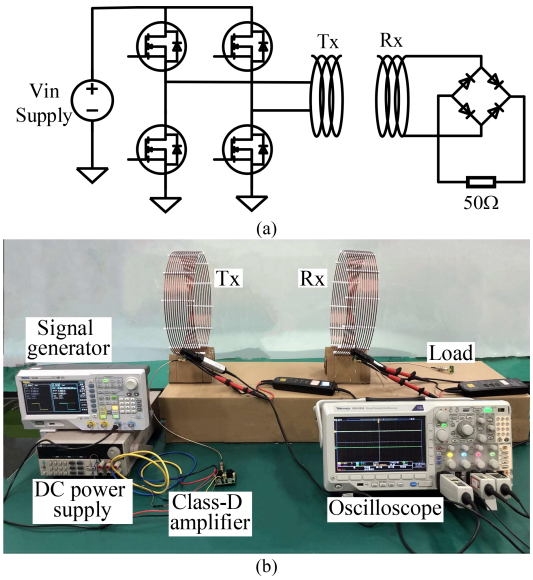

Fig. 25. (a) Diagram and (b) photograph of MRPT system prototype composed of two self-resonant coils.

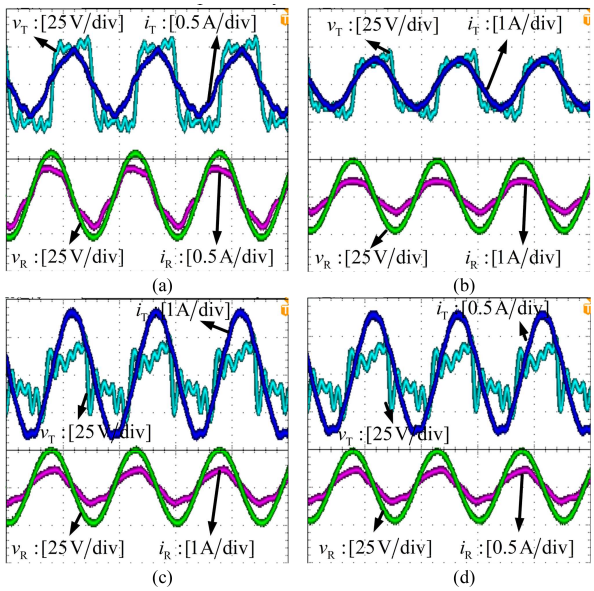

Fig. 26. Experimental waveforms at different transfer distance d_{TR}. (a) $d_{\mathrm{TR}} = 30$ cm. (b) $d_{\mathrm{TR}} = 40$ cm. (c) $d_{\mathrm{TR}} = 50$ cm. (d) $d_{\mathrm{TR}} = 60$ cm.

When the normalized transfer distance $d_{\mathrm{TR}}/d_{\mathrm{H}}$ is 2, the transfer efficiency η_{t} is still 45%.

C. Demonstration

In order to validate the power transfer capability, an experiment is carried out in the laboratory, as shown in Fig. 25. A differential mode Class-D amplifier using GaN FETs is connected to the DC source to power the Tx, and a signal generator is used as the driver of the Class-D amplifier. A 50 Ω resistance connected with a bridge rectifier is employed as the load for the Rx.

The output power is set at 5W. Measured by an oscilloscope, the experimental waveforms with four different transfer distances are shown in Fig. 26. The transfer efficiency is 90.6%, 79.5%, 59.1% and 43.2% when the transfer distance d_{TR} is 30, 40, 50 and 60 cm, respectively.

VI. Conclusion

In this paper, a precise modeling and design guideline of self-resonant helical coils for high-efficiency mid-range WPT system is established. The equivalent circuit for IPT system is built and a simple and intuitive understanding of the transfer characteristics of MRPT system is obtained. Instead of equating the self-resonant coil into a lumped inductance, the PEEC method is applied to the self-resonant coil to calculate the SRFs and the current distributions along the coil. Three simple helical coils are calculated, simulated, fabricated and measured. The errors between the PEEC calculation predications and the HFSS simulation values do not exceed 4%. And the errors relative to VNA measurement values are not greater than 10%. Furthermore, the magnetic coupling mechanism between two self-resonant helical coils is also modeled using PEEC method. Based on the above model, a design guideline for self-resonant coils is given. A couple of 6.78 MHz self-resonant helical coils are designed and fabricated for MRPT system. In order to verify that the MRPT system can transfer considerable power over a medium distance, a 50 Ω load resistance is driven wirelessly as a demonstration. Setting the output power at 5W, the transfer efficiency is 90.6% $\sim$ 43.2% when the normalized transfer distance $d_{\mathrm{TR}}/d_{\mathrm{H}}$ is between 1 and 2.

References

[1] K. Agarwal, R. Jegadeesan, Y. X. Guo, and N. V. Thakor, "Wireless power transfer strategies for implantable bioelectronics," *IEEE Rev. Biomed. Eng.*, vol. 10, pp. 136–161, 2017.

[2] Y. Jiang, M. Wu, S. Yin, Z. Wang, L. Wang, and Y. Wang, "An optimized parameter design method of WPT system for EV charging based on optimal operation frequency range," in *Proc. IEEE Appl. Power Electron. Conf. Expo.*, 2019, pp. 1528–1532, doi: 10.1109/APEC.2019.8722193.

[3] Z. Zhang, A. Georgiadis, and C. Cecati, "Wireless power transfer for smart industrial and home applications," *IEEE Trans. Ind. Electron.*, vol. 66, no. 5, pp. 3959–3962, May 2018.

[4] Y. Jiang, L. Wang, Y. Wang, J. Liu, X. Li, and G. Ning, "Analysis, design, and implementation of accurate ZVS angle control for EV battery charging in wireless high-power transfer," *IEEE Trans. Ind. Electron.*, vol. 66, no. 5, pp. 4075–4085, May 2019, doi: 10.1109/TIE.2018.2795523.

[5] M. Meng and M. Kiani, "Design and optimization of ultrasonic wireless power transmission links for millimeter-sized biomedical implants," *IEEE Trans. Biomed. Circuits Syst.*, vol. 11, no. 1, pp. 98–107, Feb. 2017.

[6] J. Garnica, R. A. Chinga, and J. Lin, "Wireless power transmission: From far field to near field," *Proc. IEEE*, vol. 101, no. 6, pp. 1321–1331, Jun. 2013.

[7] C. R. Valenta and G. D. Durgin, "Harvesting wireless power: Survey of energy-harvester conversion efficiency in far-field, wireless power transfer systems," *IEEE Microw. Mag.*, vol. 15, no. 4, pp. 108–120, Jun. 2014.

[8] M. Xia and S. Aïssa, "On the efficiency of far-field wireless power transfer," *IEEE Trans. Signal Process.*, vol. 63, no. 11, pp. 2835–2847, Jun. 2015.

[9] A. Massa, G. Oliveri, F. Viani, and P. Rocca, "Array designs for long-distance wireless power transmission: State-of-the-art and innovative solutions," *Proc. IEEE*, vol. 101, no. 6, pp. 1464–1481, Jun. 2013.

[10] Z. Zhang, H. Pang, A. Georgiadis, and C. Cecati, "Wireless power transfer - an overview," *IEEE Trans. Ind. Electron.*, vol. 66, no. 2, pp. 1044–1058, Feb. 2019.

[11] I. Mayordomo, T. Drager, P. Spies, J. Bernhard, and A. Pflaum, "An overview of technical challenges and advances of inductive wireless power transmission," *Proc. IEEE*, vol. 101, no. 6, pp. 1302–1311, Jun. 2013.

[12] A. Kurs, A. Karalis, R. Moffatt, J. D. Joannopoulos, P. Fisher, and M. Soljačić, "Wireless power transfer via strongly coupled magnetic resonances," *Science,* vol. 317, no. 5834, pp. 83–86, 2007.

[13] S. Y. R. Hui, W. Zhong, and C. K. Lee, "A critical review of recent progress in mid-range wireless power transfer," *IEEE Trans. Power Electron.*, vol. 29, no. 9, pp. 4500–4511, Sep. 2014.

[14] Y. Li, S. Jiang, J. Liu, X. Ni, R. Wang, and J. Ma, "Maximizing transfer distance for WPT via coupled magnetic resonances by coupling coils design and optimization," *IEEE Access*, vol. 8, pp. 74157–74166, 2020.

[15] C. Cheng et al., "Load-independent wireless power transfer system for multiple loads over a long distance," *IEEE Trans. Power Electron.*, vol. 34, no. 9, pp. 9279–9288, Sep. 2019.

[16] S. Y. R. Hui, "Magnetic resonance for wireless power transfer [A Look Back]," *IEEE Power Electron. Mag.*, vol. 3, no. 1, pp. 14–31, Mar. 2016.

[17] K. Lee and S. H. Chae, "Comparative study of achievable efficiency between three-coil and four-coil wireless power transfer systems," *IEEE J. Emerg. Sel. Topics Power Electron.*, vol. 10, no. 2, pp. 2138–2146, Apr. 2022.

[18] K. Wang, B. Li, Z. Qi, L. Wang, X. Yang, and A. Qiu, "Evaluation of frequency-dependent on-resistance of GaN devices at high frequency," in *Proc. 10th Int. Conf. Power Electron. ECCE Asia*, 2019 pp. 2153–2157.

[19] C. Yang, Y. Pei, L. Wang, L. Yu, F. Zhang, and B. Ferreira, "Overvoltage and oscillation suppression circuit with switching losses optimization and clamping energy feedback for SiC MOSFET," *IEEE Trans. Power Electron.*, vol. 36, no. 12, pp. 14207–14219, Dec. 2021.

[20] S. Aldhaher, D. C. Yates, and P. D. Mitcheson, "Load-independent class E/EF inverters and rectifiers for mhz-switching applications," *IEEE Trans. Power Electron.*, vol. 33, no. 10, pp. 8270–8287, Oct. 2018.

[21] H. C. Yun, G. Lee, and W. S. Park, "Empirical formulas for self resonance frequency of archimedean spiral coils and helical coils," in *Proc. IEEE Int. Symp. Antennas Propag.*, Chicago, IL, USA, 2012, pp. 1–2.

[22] A. Ayachit and M. K. Kazimierczuk, "Self-capacitance of single-layer inductors with separation between conductor turns," *IEEE Trans. Electromagn. Compat.*, vol. 59, no. 5, pp. 1642–1645, Oct. 2017.

[23] J. Li and D. Costinett, "Analysis and design of a series self-resonant coil for wireless power transfer," in *Proc. IEEE Appl. Power Electron. Conf. Expo.*, 2018, pp. 1052–1059.

[24] C. Jiang, D. E. Gaona, Y. Shen, H. Zhao, K. T. Chau, and T. Long, "Low-frequency medium power capacitor-free self-resonant wireless power transfer," *IEEE Trans. Ind. Electron.*, vol. 68, no. 11, pp. 10521–10533, Nov. 2021.

[25] T. Imura, H. Okabe, T. Uchida, and Y. Hori, "Study on open and short end helical antennas with capacitor in series of wireless power transfer using magnetic resonant couplings," in *Proc. 35th Annu. Conf. IEEE Ind. Electron.*, 2009, pp. 3848–3853.

[26] Z. Yi, M. Li, B. Muneer, and Q. Zhu, "High-efficiency mid-range inductive power transfer employing alternative-turn coils," *IEEE Trans. Power Electron.*, vol. 34, no. 7, pp. 6706–6721, Jul. 2019.

[27] Z. Yi, M. Li, B. Muneer, G. He, and X.-X. Yang, "Self-resonant antisymmetric planar coil for compact inductive power transfer system avoiding compensation circuits," *IEEE Trans. Power Electron.*, vol. 36, no. 5, pp. 5121–5134, May 2021.

[28] K. Furusato, T. Imura, and Y. Hori, "Design of multi-frequency coil for capacitor-less wireless power transfer using high order self-resonance of open end coil," in *Proc. IEEE Wireless Power Transfer Conf.*, 2016, pp. 5–8.

[29] P. Scholz, "Analysis and numerical modeling of inductively coupled antenna systems," Ph.D. dissertation, Institut für Theorie Elektromagnetischer Felder, Technische Universität Darmstadt, Darmstadt, Germany, 2010.

[30] B. Breitkreutz and H. Henke, "Calculation of self-resonant spiral coils for wireless power transfer systems with a transmission line approach," *IEEE Trans. Magn.*, vol. 49, no. 9, pp. 5035–5042, Sep. 2013.

[31] C.-J. Chen et al., "A study of loosely coupled coils for wireless power transfer," *IEEE Trans. Circuits Syst. II Exp. Briefs*, vol. 57, no. 7, pp. 536–540, Jul. 2010.

[32] M. Kiani and M. Ghovanloo, "The circuit theory behind coupled-mode magnetic resonance-based wireless power transmission," *IEEE Trans. Circuits Syst. I: Regular Papers*, vol. 59, no. 9, pp. 2065–2074, Sep. 2012.

[33] C. Carretero, J. Acero, and R. Alonso, "TM-TE decomposition of power losses in multi-stranded litz-wires used in electronic devices," *Prog. Electromagnetics Res.*, vol. 123, pp. 83–103, 2012.

Lei Zhu (Student Member, IEEE) was born in Anhui, China, in 1995. She received the B.S. degree in electrical engineering from Xi'an Jiaotong University, Xi'an, China, in 2018. She is currently working toward the Ph.D. degree in School of Electrical Engineering, Xi 'an Jiaotong University. Her research interests include wireless power transfer, high frequency, and high power density dc–dc converters, signal processing, and digital control technology.

Laili Wang (Senior Member, IEEE) was born in Shaanxi province, China, in 1982. He received the B.S., M.S., and Ph.D. degrees in electrical engineering from Xi'an Jiaotong University, Xi'an, China, in 2004, 2007, and 2011, respectively. Since 2011, he has been a Postdoctoral Research Fellow with the Department of Electrical Engineering, Queen's University, Kingston, ON, Canada. From 2014 to 2017, he was an Electrical Engineer with Sumida, Canada. In 2017, he joined Xi'an Jiaotong University as a Professor. His research interests include package and integration of passive devices in high-frequency high power density dc–dc converters, wireless power transfer, and energy harvesting.

Min Wu (Student Member, IEEE) was born in Sichuan, China, in 1995. He received the B.S. degree in electrical automatization from Chongqing University, Chongqing, China, in 2017. He is currently working toward the Ph.D. degree in electrical engineering and automation with Xi'an Jiaotong University, Xi'an, China. His research interest is wireless power transfer and high-frequency power converter.

Chenxu Zhao (Student Member, IEEE) was born in Heilongjiang, China, in 1996. He received the B.S. degree in electrical automatization from Northwestern Polytechnical University, Xi'an, China, in 2019. He is currently working toward the Ph.D. degree in electrical engineering in Xi'an Jiaotong University, Xi'an, China. His research interests include high frequency wireless power transfer systems and GaN-based converters.

Longyang Yu (Student Member, IEEE) was born in 1992. He received the B.S. degree in electrical engineering from Xi'an university of technology, Shaanxi, China, in 2015, and the Ph.D. degree in electrical engineering at Xi'an Jiaotong University, Xi'an, China, in 2022. He has been a Lecturer in Xidian University, Xi'an, China, in 2022. His research interests include power electronic topology, applications of GaN devices and high frequency magnetic component integration.